JNeurosci
THE JOURNAL OF NEUROSCIENCE

Research Articles: Neurobiology of Disease

Decreased axon caliber underlies loss of fiber tract integrity, disproportional reductions in white matter volume, and microcephaly in Angelman syndrome model mice

Matthew C. Judson[1,2], Alain C. Burette[1], Courtney L. Thaxton[1,2], Alaine L. Pribisko[1], Mark D. Shen[2], Ashley M. Rumple[3], Wilmer A. Del Cid[1,4], Beatriz Paniagua[3], Martin Styner[3], Richard J. Weinberg[1,5] and Benjamin D. Philpot[1,2,5]

[1]*Department of Cell Biology and Physiology, University of North Carolina, Chapel Hill, 27599*
[2]*Carolina Institute for Developmental Disabilities, University of North Carolina, Chapel Hill, 27599*
[3]*Department of Psychiatry, University of North Carolina, Chapel Hill, 27599*
[4]*Postbaccalaureate Research Education Program, University of North Carolina, Chapel Hill, 27599*
[5]*Neuroscience Center, University of North Carolina, Chapel Hill, 27599*

DOI: 10.1523/JNEUROSCI.0037-17.2017

Received: 5 January 2017

Revised: 24 May 2017

Accepted: 21 June 2017

Published: 29 June 2017

Author contributions: M.C.J., A.B., C.T., A.L.P., M. Shen, A.R., W.D.C., B.P., M. Styner, R.J.W., and B.D.P. designed research; M.C.J., A.B., C.T., A.L.P., M. Shen, A.R., W.D.C., and B.P. performed research; M.C.J., A.B., C.T., A.L.P., M. Shen, A.R., W.D.C., B.P., and M. Styner analyzed data; M.C.J., A.B., C.T., A.L.P., M. Shen, R.J.W., and B.D.P. wrote the paper.

Conflict of Interest: The authors declare no competing financial interests.

We thank Ji Eun Han and Hyojin Kim for help genotyping and maintaining animal colonies, and Kristen Phend for histological support. This work was supported by NRSA fellowship 5F32NS077686 (to M.C.J.), Angelman Syndrome Foundation grants (to B.D.P.), NINDS 5RO1NS039444 (to R.J.W.), and NINDS 1RO1NS085093 (to B.D.P.). Confocal imaging was supported by NINDS Center Grant P30 NS045892 and NICHD Center Grant P30 HD03110.

Correspondence: Ben Philpot, 115 Mason Farm Rd., Campus Box 7545, Chapel Hill, NC 27599 P:(919) 966-0025, F:(919) 966-3870, bphilpot@med.unc.edu

Cite as: J. Neurosci ; 10.1523/JNEUROSCI.0037-17.2017

Decreased axon caliber underlies loss of fiber tract integrity, disproportional reductions in white matter volume, and microcephaly in Angelman syndrome model mice

Matthew C. Judson[1,2], Alain C. Burette[1‡], Courtney L. Thaxton[1,2‡], Alaine L. Pribisko[1], Mark D. Shen[2], Ashley M. Rumple[3], Wilmer A. Del Cid[1,4], Beatriz Paniagua[3], Martin Styner[3], Richard J. Weinberg[1,5], and Benjamin D. Philpot[1,2,5,*]

[1]Department of Cell Biology and Physiology, University of North Carolina, Chapel Hill, 27599
[2]Carolina Institute for Developmental Disabilities, University of North Carolina, Chapel Hill, 27599
[3]Department of Psychiatry, University of North Carolina, Chapel Hill, 27599
[4]Postbaccalaureate Research Education Program, University of North Carolina, Chapel Hill, 27599
[5]Neuroscience Center, University of North Carolina, Chapel Hill, 27599
[‡]These authors contributed equally to this work.

***Correspondence:** Ben Philpot, 115 Mason Farm Rd., Campus Box 7545, Chapel Hill, NC 27599
P:(919) 966-0025, F:(919) 966-3870, bphilpot@med.unc.edu

Number of Pages: 42
Number of Figures: 11
Number of Tables: 2
Number of Words: Abstract (144), Introduction (463), Discussion (1486)

CONFLICT OF INTEREST STATEMENT
The authors declare that they have no competing financial interests.

ACKNOWLEDGEMENTS
We thank Ji Eun Han and Hyojin Kim for help genotyping and maintaining animal colonies, and Kristen Phend for histological support. This work was supported by NRSA fellowship 5F32NS077686 (to M.C.J.), Angelman Syndrome Foundation grants (to B.D.P.), NINDS 5RO1NS039444 (to R.J.W.), and NINDS 1RO1NS085093 (to B.D.P.). Confocal imaging was supported by NINDS Center Grant P30 NS045892 and NICHD Center Grant P30 HD03110.

Abbreviated Title: **The basis of microcephaly in AS**

ABSTRACT

Angelman syndrome (AS) is a debilitating neurodevelopmental disorder caused by loss of function of the maternally inherited *UBE3A* allele. It is currently unclear how the consequences of this genetic insult unfold to impair neurodevelopment. We reasoned that by elucidating the basis of microcephaly in AS – a highly penetrant syndromic feature with early postnatal onset – we would gain new insights into the mechanisms by which maternal *UBE3A* loss derails neurotypical brain growth and function. Detailed anatomical analysis of both male and female maternal *Ube3a*-null mice reveals that microcephaly in the AS mouse model is primarily driven by deficits in the growth of white matter tracts, which by adulthood are characterized by densely-packed axons of disproportionately small caliber. Our results implicate impaired axon growth in the pathogenesis of AS, and identify noninvasive structural neuroimaging as a potentially valuable tool for gauging therapeutic efficacy in the disorder.

SIGNIFICANCE STATEMENT: People who maternally inherit a deletion or nonfunctional copy of the *UBE3A* gene develop Angelman syndrome (AS), a severe neurodevelopmental disorder. To better understand how loss of maternal *UBE3A* function derails brain development, we analyzed brain structure in a maternal *Ube3a* knockout mouse model of AS. We report that the volume of white matter is disproportionately reduced in AS mice, indicating that deficits in white matter development are a major factor underlying impaired brain growth and microcephaly in the disorder. Notably, we find that axons within the white matter pathways of AS model mice are abnormally small in caliber. This defect is associated with slowed nerve conduction, which could contribute to behavioral deficits in AS, including motor dysfunction.

INTRODUCTION

Maternally inherited deletions or mutations of *UBE3A* cause Angelman syndrome (AS), a severe neurodevelopmental disorder (Kishino et al., 1997; Matsuura et al., 1997; Sutcliffe et al., 1997). Individuals with AS suffer from profound developmental delay, impaired motor function, absence of speech, and other highly penetrant phenotypes including electroencephalographic abnormalities, epilepsy, and microcephaly (Mabb et al., 2011; Margolis et al., 2015). These features of AS begin to manifest during the first year of life (Fryburg et al., 1991; Dagli et al., 2012), indicating an early deviation from the typical course of neurodevelopment.

Not all brain cells express *UBE3A* equally, lending traction to efforts geared toward deciphering altered neurodevelopmental trajectories in AS. Due to cell type-specific epigenetic mechanisms, neuronal expression of *UBE3A* from the paternal allele is silenced during early phases of cellular differentiation and maturation (Rougeulle et al., 1997; Yamasaki et al., 2003), thereby rendering neurons especially vulnerable to the maternal *UBE3A* loss that defines AS. In contrast, paternal *UBE3A* expression is spared in neural stem cells and in glia, which biallelically express the gene (Yamasaki et al., 2003; Judson et al., 2014). Neurons are therefore an obvious focal point for AS research, but due to the spatiotemporal ubiquity of *UBE3A* expression throughout development (Judson et al., 2014; Burette et al., 2016), virtually any neuron or neural circuit could contribute to AS pathogenesis through a variety of primary deficits in neuronal physiology – a daunting possibility.

UBE3A (also called E6-AP) is the founding member of the HECT (homologous to the E6-AP carboxyl terminus) domain family of E3 ubiquitin ligases, which can catalyze the polyubiquitination of substrate proteins, targeting them for proteasomal degradation (Mabb and

Ehlers, 2010; Mabb et al., 2011). UBE3A can also act as a transcriptional co-activator (Nawaz et al., 1999; Reid et al., 2003; El Hokayem and Nawaz, 2014), but mutations that selectively inhibit its ubiquitin ligase activity are sufficient to cause AS (Cooper et al., 2004), implying that improper substrate regulation in neurons is the primary pathogenic basis of the disorder. Candidate UBE3A substrates and other UBE3A-interacting proteins in neurons continue to be identified, but clear and direct links to specific phenotypes remain elusive (Sell and Margolis, 2015).

Here we sought to elucidate the anatomical underpinnings of microcephaly in AS, operating on the premise that better understanding the causes of impaired brain growth in the disorder would yield new insights into the neurodevelopmental consequences of maternal *UBE3A* loss in neurons. Toward this end, we brought the complementary approaches of structural neuroimaging, light and electron microscopy, and electrophysiology to bear in AS model mice. We conclude that deficits in brain growth consequent to maternal *UBE3A* loss are likely the product of disproportionate reductions in white matter (WM) volume, rooted in the failure of projection neurons to develop axons of appropriate caliber.

MATERIALS AND METHODS

Animals

We raised all mice on a 12:12 light:dark cycle with *ad libitum* access to food and water, and performed all experiments in strict compliance with animal protocols approved by the Institutional Animal Care and Use Committees of the University of North Carolina at Chapel Hill. We used both male and female littermates at equivalent genotypic ratios, with the exception of brain and body weight measures (Figure 1), for which we analyzed only female mice at P28 and P90, to control for the sexual dimorphism in body weight. Mice carrying the *Ube3a* knockout allele were originally generated in the laboratory of A. Beaudet (Jiang et al., 1998), and back-crossed to a congenic C57BL/6J background (RRID:IMSR_JAX:016590). We generated maternal *Ube3a*-deficient mice (*Ube3a*$^{m-/p+}$) by crossing congenic C57BL/6 wildtype males to paternal *Ube3a*-deficient females (*Ube3a*$^{m+/p-}$), which themselves are phenotypically normal (Jiang et al., 1998; Mulherkar and Jana, 2010). To generate mice for the analysis of cortical area patterning (see below), we crossed *Ube3a*$^{m+/p-}$ females to male homozygous *Ai9*, tdTomato Cre-reporter mice (Madisen et al., 2010), which were also maintained on a congenic C57BL/6 background (RRID:IMSR_JAX:007909).

Diffusion Tensor Imaging (DTI) and Analysis

Tissue Preparation: We deeply anesthetized P90 mice with sodium pentobarbital (60 mg/kg i.p.) prior to transcardially perfusing them with heparinized saline (0.9% NaCl, 10 IU heparin/ml), immediately followed by phosphate-buffered 4% paraformaldehyde (pH 7.3) at a rate of 9 ml/min. After delivering 50 ml of fixative, we decapitated mice, postfixed their heads

overnight at 4°C, and rinsed and stored them in phosphate-buffered saline (PBS) at 4°C prior to imaging.

Image Acquisition and Processing: We acquired diffusion-weighted images (24 directions; b-value = 1600; FOV = 200 x 256 x 128; voxel resolution = 0.12 x 0.12 x 0.12 mm^3; TE = 22.75 ms; TR = 700 ms; scan time = 15 hours) using a 9.4T scanner at the UNC Small Animal Imaging Facility (BioSpec 9.4/30 USR, Bruker Biospin, Billerica, MA). We processed images using an in-house pipeline developed by our laboratory at UNC, which utilizes unbiased, atlas-based, regional segmentation (Budin et al., 2013). First, we rigidly registered the images to the C57 Brookhaven atlas (Ma et al., 2005) in order to align them in a common space. We then skull-stripped the images and performed histogram matching and affine registration, creating a population average image using AtlasWerks (Joshi et al., 2004). We diffeomorphically registered a parcellation of brain regions (based on the Brookhaven Atlas) to the population average image using ANTS (Avants et al., 2008), allowing us to propagate the population average segmentation to the individual case images and generate regional statistics. A single anatomical expert, blind to sex and genotype, visually checked each case for quality control.

Volumetric Segmentation: We performed WM volumetric segmentations on the RD image of each individual case in ITK-SNAP (RRID:SCR_002010) (Yushkevich et al., 2006), according to the following parameters: corpus callosum, segmented in 4 contiguous sagittal slices at the midline (defined by the presence of the superior sagittal sinus; internal capsule, segmented primarily in the coronal plane, with an anterior boundary at the body of the anterior commissure

and a posterior boundary at the ascending limb of the stria terminalis; anterior commissure, segmented primarily in the horizontal plane, with an anterior boundary for the anterior limbs at the genu of the corpus callosum and a posterior boundary at the optic chiasm; fimbria, segmented in its entirety, primarily in the coronal plane; fornix, segmented primarily in the coronal plane, with the boundary for the precommissural fornix two slices anterior to the body of the anterior commissure and the boundary for the postcommissural fornix 3 slices anterior to the mammillary bodies.

We segmented the cerebral cortex using the propagated atlas parcellation. Cortical segmentations were automatically eroded by one voxel to eliminate the partial voluming of voxels between the outer pial surface of cortex and the subarachnoid space. An anatomical expert, blind to sex and genotype, visually inspected each case and manually edited the cortical segmentation using ITK-Snap.

DTI Data Processing and Tractography: We processed DTI data according to procedures that provide consistent parameterization between subjects (Goodlett et al., 2009), generating a final average tensor atlas of all *Ube3a*$^{m-/p+}$ and littermate control brains. Working from this average atlas, we performed tractography for each tract of interest through seed label mapping in 3D Slicer (RRID:SCR_002579), with ITK-SNAP-generated segmentations serving as seed labels. We edited the resultant tractography-computed tracts in 3D Slicer and in FiberViewerLight, eliminating spurious and partial fibers prior to parameterization and the generation of subject-specific, tract-based statistics using DTIAtlasFiberAnalyzer (Verde et al., 2014). Finally, we performed a functional analysis of the tract-based statistics, or FADTTS (Zhu et al., 2011), using the FADTTSter tool and controlling for imaging cohort as a covariate. All of the open-

source tools constituting this DTI processing pipeline are publically available through the UNC-Utah NA-MIC DTI fiber tract analysis framework (www.nitrc.org/projects/namicdtifiber).

Electrophysiology

For nerve conduction recordings, we anesthetized mice with sodium pentobarbital (60 mg/kg) and decapitated them prior to acutely dissecting the tibial branch of the sciatic nerve. Following previously described methods (Pillai et al., 2009), we used a Ag/AgCl suction electrode in a dual-compartment *ex vivo* recording chamber to deliver rectangular wave pulses (10 μs in duration) to the proximal portion of the nerve, adjusting the stimulus amplitude (10-30 V) to ensure a near-maximal response of the large-caliber Aαβ fiber component. We calculated maximum conduction velocity by dividing the distance between the stimulating and recording electrodes (20 mm) by the conduction latency (ms from stimulus artifact to Aαβ deflection).

Light Microscopy and Analysis

Tissue Preparation: We anesthetized mice with sodium pentobarbital (60 mg/kg) prior to transcardial perfusion with PBS, immediately followed by phosphate-buffered 4% paraformaldehyde (pH 7.3). We removed perfused brains from their skulls and postfixed them overnight at 4°C prior to sequential 12-hour incubations in 10%, 20%, and 30% sucrose in PBS (pH 7.5) for cryoprotection. We then froze cryoprotected brains on dry ice and cut them into 40 μm-thick sections with a sliding microtome (Thermo Fisher Scientific, Waltham, MA). We stored sections at -20°C in a cryopreservative solution (by volume: 45% PBS, 30% ethylene glycol, 25% glycerol) until performing free-floating immunohistochemistry.

Immunohistochemistry: We rinsed sections several times in PBS before blocking in PBS plus 5% normal goat serum and 0.2% Triton-X-100 (NGST) for 1 hour at room temperature. We subsequently incubated blocked tissue sections in primary antibodies diluted in NGST for 48 hours at 4°C. We then rinsed them several times in PBS containing 0.2% Triton-X-100 (PBST) before incubation in secondary antibodies (also diluted in NGST) for 1 hour at room temperature. In most experiments, we also added 4',6-diamidino-2-phenylindole (DAPI; Thermo Fisher Scientific, Cat# D1306) at a concentration of 700 ng/ml for nuclear counterstaining. Primary antibodies and dilutions used included 1:500 mouse anti-NeuN (Millipore Cat# MAB377, RRID:AB_10048713), 1:500 rabbit anti-CUX1 (Santa Cruz Biotechnology Cat# sc-13024, RRID:AB_2261231), and 1:1000 CTIP2 (Abcam Cat#ab18465, RRID:AB_2064130). We used secondary antibodies (Thermo Fisher Scientific) at a 1:500 dilution, including Alexa-647 goat anti-mouse IgG_1 (Cat# A21240, RRID:AB_10565021), Alexa-488 goat anti-rabbit IgG (Cat# A11008, RRID:AB_10563748), and Alexa-568 goat anti-rat IgG (Cat# A11077, RRID:AB_10562719). We stained all brain sections for quantitative analysis within the same experiment, under identical conditions.

Imaging: We acquired images of immunofluorescently labeled brain sections with a Zeiss LSM 710 confocal microscope equipped with ZEN imaging Software (Zeiss, Jena, Germany, RRID:SCR_013672). We collected images for quantitative comparison during the same imaging session using identical acquisition parameters.

Analysis of Cortical Area Patterning: We generated sensory area maps for *Scnn1a-Cre::Ai9*::*Ube3a*$^{m-/p+}$ and littermate control (*Scnn1a-Cre::Ai9*::*Ube3a*$^{m+/p+}$) mice; *Scnn1a-Cre* is

expressed by L4 neurons within primary sensory areas of neocortex; the *Ai9* allele harbors a floxed STOP cassette preventing tdTomato expression from the *Gt(ROSA)26Sor* locus prior to Cre-mediated recombination (Madisen et al., 2010). Following transcardial perfusion with 2% paraformaldehyde (pH 7.3) and removal of the hippocampus and subcortical structures, we flattened the cortical hemispheres from each mouse between weighted glass slides. Subsequently, we cut hemispheres to a thickness of 40 μm and imaged 4-6 consecutive sections (15 μm optical thickness) per hemisphere in order to capture the entirety of TdTomato fluorescence in L4 sensory cortex, the boundaries of which we traced and measured using Image J software (RRID:SCR_003070) (Schneider et al., 2012).

Analysis of Cortical Laminar Patterning: We measured the percentage of primary somatosensory cortical thickness stained for CUX1 (layers 1-4; L1-4) and CTIP2 (L5-6) within 100 μm-wide sampling strips. We averaged the results from four strips per mouse, one +0.14 mm and one -0.94 mm relative to Bregma, for each hemisphere.

Analysis of Cortical Cell Density: We acquired all images for cortical cell density analyses using thin (1.4 μm-thick) optical sectioning. For each animal, we sampled four 100 μm-wide strips of primary somatosensory cortex: one +0.14 mm and one -0.94 mm relative to bregma per hemisphere. We averaged counts of both NEUN+/DAPI+ (neurons) and NEUN-/DAPI+ (glia), which we made using the cell counter plug-in in Image J. We used CUX1 and CTIP2 counterstaining to reliably subdivide L1-4 and L5-6 laminae within each strip.

Electron Microscopy and Analysis

Tissue Preparation: We sacrificed anesthetized mice (60 mg/kg sodium pentobarbital) by transcardial perfusion with 0.9% NaCl, followed immediately by fixative consisting of 2% glutaraldehyde (Electron Microscopy Science, Hatfield, PA), 2% depolymerized paraformaldehyde, and 0.2% picric acid in 0.1 M phosphate buffer (pH 6.8). We immediately removed the perfused brains and dissected the sciatic nerves, postfixed them overnight at 4°C in the same fixative, and sectioned them the following day on a vibratome to a thickness of 50 µm. We postfixed sagittal brain sections and transverse sections of sciatic nerve in 1% osmium tetroxide in 0.1 M phosphate buffer for 1 hour prior to incubation with 1% uranyl acetate in maleate buffer (0.1 M, pH 6.0) for 1 hr. After dehydration, we infiltrated the sections with Spurr resin and flat-mounted them between sheets of ACLAR® fluoropolymer within glass slides. We glued chips of corpus callosum or sciatic nerve onto plastic blocks, sectioned them en face at ~60 nm, collected them on 300 mesh nickel grids coated with Coat-Quick G, and performed poststaining with uranyl acetate and Sato's lead.

Callosal Imaging and Analysis: We performed electron microscopy on callosal material with a Tecnai 12 transmission electron microscope (Philips, Andover, MA) at 80 kV, acquiring images at 4400X magnification. We measured both unmyelinated and myelinated axon caliber (measuring specifically the axoplasmic cross-sectional area, excluding the myelin sheath) and total axon density from randomly sampled 120 μm^2 photomontages (15-20 images, 400-507 unmyelinated and 1899-2939 myelinated axons analyzed per mouse). We extrapolated axon diameters from cross-sectional area measurements, assuming a circular fit. To ensure that axons in wildtype and *Ube3a*$^{m-/p+}$ mice were equivalently circular, we analyzed the "round" and

"circularity" shape descriptor parameters within Image J, finding no significant differences between groups. We calculated g-ratios (the ratio of the inner axonal diameter to the total outer diameter axonal diameter, including the myelin sheath) from randomly sampled 15 μm^2 electron micrographs (15-20 images, 457-666 myelinated axons per mouse).

Sciatic Nerve Imaging and Analysis:

We acquired electron micrographs of the sciatic nerve with a Zeiss 910 transmission electron microscope at 80 kV, acquiring images at 1600X magnification. We measured myelinated axon caliber and g-ratios from randomly sampled ~2500 μm^2 micrographs (5-14 per mouse, totaling 404-1245 myelinated axons).

Figure Production

We linearly adjusted the brightness and contrast of some images in figure plates using Image J software. All images meant for direct comparison within figures underwent identical manipulations. We prepared all figures using Adobe Illustrator software (Adobe Systems Inc., San Jose, CA, RRID:SCR_010279).

Experimental Design and Statistical Analysis

We performed and analyzed all experiments blind to genotype, estimating minimum sample sizes from previously published datasets with similar experimental parameters. For brain and body weight, neuroimaging, light microscopy, electron microscopy, and electrophysiology experiments, we drew measurements from mutant animals and their age-matched littermates, and attempted to balance the number of animals drawn from each sex.

Sample sizes by experiment:

Body and brain growth (Figure 1): P0, 7 *Ube3a*$^{m+/p+}$ (3 males, 4 females) and 6 *Ube3a*$^{m-/p+}$ (3 males, 3 females) mice; P6, 6 *Ube3a*$^{m+/p+}$ (4 males, 2 females) and 13 *Ube3a*$^{m-/p+}$ (7 males, 6 females) mice; P7, 8 *Ube3a*$^{m+/p+}$ (3 males, 5 females) and 11 *Ube3a*$^{m-/p+}$ (4 males, 7 females) mice; P8, 10 *Ube3a*$^{m+/p+}$ (6 males, 4 females) and 7 *Ube3a*$^{m-/p+}$ (3 males, 4 females) mice; P14, 8 *Ube3a*$^{m+/p+}$ (6 males, 2 females) and 6 *Ube3a*$^{m-/p+}$ (2 males, 4 females) mice; P16, 7 *Ube3a*$^{m+/p+}$ (6 males, 1 female) and 10 *Ube3a*$^{m-/p+}$ (3 males, 7 females) mice; P28, 7 female *Ube3a*$^{m+/p+}$ and 5 female *Ube3a*$^{m-/p+}$ mice; P90, 5 female *Ube3a*$^{m+/p+}$ and 6 female *Ube3a*$^{m-/p+}$ mice.

Cortical area mapping (Figure 2C): 5 *Ube3a*$^{m+/p+}$ (2 males, 3 females) and 3 *Ube3a*$^{m-/p+}$ (1 male, 2 females) mice.

Cortical lamination (Figure 2F): 3 *Ube3a*$^{m+/p+}$ (1 male, 2 females) and 3 *Ube3a*$^{m-/p+}$ (1 male, 2 females) mice.

WM volumetrics (Table 1): 7 *Ube3a*$^{m+/p+}$ (4 males, 3 females) and 6 *Ube3a*$^{m-/p+}$ (3 males, 3 females) mice.

WM/GM ratios (Figures 3 and 4): 7 *Ube3a*$^{m+/p+}$ (4 males, 3 females) and 5 *Ube3a*$^{m-/p+}$ (3 males, 2 females) mice.

DTI tractography (Figure 5 and Table 2): 7 *Ube3a*$^{m+/p+}$ (4 males, 3 females) and 6 *Ube3a*$^{m-/p+}$ (3 males, 3 females) mice.

Callosal electron microscopy (Figures 6, 7, and 8): 6 *Ube3a*$^{m+/p+}$ (2 males, 4 females) and 6 *Ube3a*$^{m-/p+}$ (2 males, 4 females) mice.

318 *Cortical cell density (Figure 9)*: 3 *Ube3a*$^{m+/p+}$ (1 male, 2 females) and 3 *Ube3a*$^{m-/p+}$
319 (1 male, 2 females) mice.
320 *Sciatic nerve electron microscopy (Figures 10A-10C and 11)*: 6 *Ube3a*$^{m+/p+}$ (3 males, 3
321 females) and 6 *Ube3a*$^{m-/p+}$ (3 males, 3 females) mice.
322 *Sciatic nerve conduction (Figure 10F-10H)*: 6 *Ube3a*$^{m+/p+}$ (3 males, 3 females) and 6
323 *Ube3a*$^{m-/p+}$ (3 males, 3 females) mice.
324
325 We performed statistical analyses using GraphPad Prism 6 (GraphPad Software Inc., La Jolla,
326 CA, RRID:SCR_002798), SPSS 22 (IBM, Armonk, NY, RRID:SCR_002865), and the
327 FADTTSter tool (www.nitrc.org/projects/namicdtifiber).
328
329 ***Statistical analyses by experiment:***
330 *Body and brain growth (Figure 1)*: two-way ANOVA, Sidak's post-hoc test.
331 *Cortical area mapping (Figure 2C)*: two-way ANOVA, Sidak's post-hoc test.
332 *Cortical lamination (Figure 2F)*: Unpaired two-tailed t-test.
333 *WM volumetrics (Table 1)*: MANCOVA, setting imaging cohort as the covariate.
334 *WM/GM ratios (Figures 3 and 4)*: Unpaired two-tailed t-test.
335 *DTI tractography (Figure 5D and Table 2)*: FADTTS.
336 *Callosal electron microscopy*: Unpaired two-tailed t-test (*Figures 6B, 6E, 6G, and 8A*)
337 and two-way repeated measures ANOVA, Sidak's post-hoc test
338 (*Figures 6F, 7A, 7B, 8B, and 8C*).
339 *Cortical cell density (Figure 9C-9G)*: Unpaired two-tailed t-test.
340 *Sciatic nerve electron microscopy*: Unpaired two-tailed t-test (*Figures 10B and 11A*) and

two-way repeated measures ANOVA, Sidak's post-hoc test (*Figures 10C and 11C*).

Sciatic nerve conduction (Figure 10F-10H): Unpaired two-tailed t-test.

RESULTS

Microcephaly in *Ube3a*$^{m-/p+}$ mice is associated with a disproportionate loss of WM volume

Individuals with AS are born with normal head circumference, but present with absolute microcephaly – decreased head circumference irrespective of body size – within the first 8-12 months of life (Dagli et al., 2012). The emergence of microcephaly coincides with the manifestation of early neurological phenotypes, including truncal hypotonia and seizures (Fryburg et al., 1991; Dagli et al., 2012), suggesting a close link between deficits in early postnatal brain growth and AS pathophysiology. To determine whether mice lacking a functional maternal *Ube3a* copy (*Ube3a*$^{m-/p+}$, AS model mice) exhibit microcephaly according to a similar time course, we tracked brain weight cross-sectionally over postnatal development. *Ube3a*$^{m-/p+}$ brain growth appeared normal at birth through postnatal day (P) 8, but then the trajectory flattened relative to control, leading to statistically significant group deficits by P14 (Figure 1A and 1B [two-way ANOVA for genotype x age interaction, $F(7, 106) = 4.38$, $p = 0.0003$; *post hoc* unpaired t-test with Sidak's multiple comparisons correction, $t(106) = 5.11$, $p < 0.0001$]). In contrast, body weights in *Ube3a*$^{m-/p+}$ and control mice were similar up to P90, when *Ube3a*$^{m-/p+}$ mice showed evidence of adult-onset obesity (Figure 1C [two-way ANOVA for genotype x age interaction, $F(7, 106) = 4.76$, $p = 0.0001$; *post hoc* unpaired t-test with Sidak's multiple comparisons correction, $t(106) = 5.33$, $p < 0.0001$]), consistent with previous

reports in mice and with clinical reports of adults with AS (van Woerden et al., 2007; Dagli et al., 2012; Huang et al., 2013; Margolis et al., 2015). Thus, *Ube3a*$^{m-/p+}$ mice faithfully model absolute microcephaly with early postnatal onset, as is observed in AS.

Postnatally-emergent microcephaly suggests a sparing of prenatal ontogenetic processes governing brain histogenesis. Accordingly, we found grossly normal cortical patterning in *Ube3a*$^{m-/p+}$ mice: sensory area maps (Figure 2A-2C [two-way ANOVA, $F(2, 18 = 4.38$, $p = 0.1758$]) and lamination (Figure 2D-2F [L1-4 unpaired two-tailed t-test, $t(4) = 0.45$, $p = 0.68$; L5-6 unpaired two-tailed t-test, $t(4) = 0.45$, $p = 0.68$]) were appropriately proportioned and indistinguishable from control. To uncover further clues as to how postnatal brain growth is affected by the loss of maternal *Ube3a*, we undertook a detailed MRI-based volumetric analysis of the *Ube3a*$^{m-/p+}$ brain. Brain structures comprising mostly gray matter were somewhat smaller in *Ube3a*$^{m-/p+}$ mice than in littermate controls at P90. In *Ube3a*$^{m-/p+}$ cerebral cortex, for example, volumes were reduced by an average of 7% (Figure 3A-C [unpaired two-tailed t-test, t(10) = 3.34, $p = 0.008$]). However, we observed larger reductions in the volume of WM tracts within the *Ube3a*$^{m-/p+}$ brain. Each tract that we analyzed was at least 11% smaller than control: corpus callosum showed the greatest volumetric difference, -13.5% (Table 1). We subsequently verified that WM volume is disproportionately reduced in *Ube3a*$^{m-/p+}$ mice via ratiometric comparison of WM tract volumes with volumes for total cortex, forebrain, and whole brain in each animal (Figures 3D, 3E, and 4 [unpaired two-tailed t-tests: callosum:cortex, $t(10) = 2.5$, $p = 0.03$; callosum:forebrain, $t(10) = 2.83$, $p = 0.02$; callosum:whole brain, $t(10) = 3.32$, $p = 0.008$; capsule:cortex, $t(10) = 3.93$, $p = 0.003$; capsule:forebrain, $t(10) = 4.87$, $p = 0.0007$; capsule:whole brain, $t(10) = 6.43$, $p < 0.0001$; commissure:forebrain, $t(10) = 2.78$, $p = 0.02$; commissure:wholebrain, $t(10) = 3.03$, $p = 0.01$;

fornix:forebrain, $t(10) = 1.3$, $p = 0.22$; fornix:whole brain, $t(10) = 1.56$, $p = 0.15$; fimbria:forebrain, $t(10) = 1.73$, $p = 0.11$; fimbria:wholebrain, $t(10) = 1.96$, $p = 0.08$]).

WM integrity is globally compromised in the adult *Ube3a*$^{m-/p+}$ brain

We next investigated whether WM volumetric deficits were accompanied by microstructural abnormalities. DTI tractography of the corpus callosum (Figure 5A-5C) revealed a pronounced decrease in axial diffusivity (AD) along the entire mediolateral extent of the tract in *Ube3a*$^{m-/p+}$ mice compared to control, whereas radial diffusivity (RD) was unperturbed (Figure 5D and 5E). Thus, reductions in AD drove the decreases in mean diffusivity (MD) and fractional anisotropy (FA) that we observed for the corpus callosum (Figure 5D and 5E). All tracts that we analyzed exhibited highly significant statistical effects for both AD and MD except the precommissural fornix, where decreases in AD only approached significance (Table 2). Unlike other tracts, the precomissural fornix, postcommissural fornix, and the fimbria consistently showed decreases in RD along with decreases in AD. This likely explains the lack of significant FA effects in these major efferent pathways of the hippocampus, as FA is sensitive to the disproportionality of AD and RD. We therefore conclude that compromised WM integrity – in particular, reduced AD – is a general feature of WM tracts in the adult *Ube3a*$^{m-/p+}$ brain.

Decreased axon caliber underlies altered WM microstructure in adult *Ube3a*$^{m-/p+}$ mice

A number of axonal abnormalities could lead to reduced AD within WM tracts (Mori and Zhang, 2006). We performed electron microscopy to determine factors that could explain AD deficits in *Ube3a*$^{m-/p+}$ mice. Focusing on the anterior midbody of the corpus callosum, myelination appeared grossly normal (Figure 6A), consistent with a lack of RD deficits within this tract

(Figure 5E and Table 2) (Song et al., 2002; Song et al., 2005). Although average g-ratios for *Ube3a*$^{m-/p+}$ callosal axons were slightly decreased relative to control (Figure 6B [unpaired two-tailed t-test, $t(10) = 2.47$, $p = 0.03$]), plots of axon diameter versus g-ratio suggested that this did not reflect enhanced myelination in *Ube3a*$^{m-/p+}$ mice (Figure 6C), but rather an underrepresentation of large-caliber axons (Figure 7A [two-way ANOVA for genotype x diameter interaction, $F(3, 30) = 4.43$, $p = 0.01$; *post hoc* unpaired t-test with Sidak's multiple comparisons correction, $t(40) = 4.11$, $p = 0.0008$]), which tend to have higher g-ratios. Indeed, we found that the caliber of myelinated axons was markedly affected in the adult *Ube3a*$^{m-/p+}$ callosum: cross-sectional area was decreased by ~25% on average (Figure 6D and 6E [unpaired two-tailed t-test, $t(10) = 5.1$, $p = 0.0005$]), and we observed a leftward skew in the distribution of diameters (Figure 6F [two-way repeated measures ANOVA for genotype x diameter interaction, $F(17, 170) = 6.01$, $p < 0.0001$]; Figure 7B [two-way repeated measures ANOVA for genotype x diameter interaction, $F(3, 30) = 14.02$, $p < 0.0001$]), indicating reduced caliber in both large and small myelinated axons. Reductions in the caliber of unmyelinated callosal axons were much more modest and did not achieve statistical significance (Figure 8A [unpaired two-tailed t-test, $t(10) = 2.09$, $p = 0.06$]; Figure 8B [two-way repeated measures ANOVA for genotype x diameter interaction, $F(15, 150) = 1.18$, $p = 0.3$]; Figure 8C [two-way repeated measures ANOVA for genotype x diameter interaction, $F(4, 40) = 1.1$, $p = 0.37$), suggesting that loss of maternal *Ube3a* may preferentially affect the growth of myelinated axons.

Fewer axons or axon collaterals could also compromise WM integrity, but we found that axon packing density was actually increased by ~25% in the callosum of *Ube3a*$^{m-/p+}$ mice (Figure 6G [unpaired two-tailed t-test, $t(10) = 3.15$, $p = 0.01$]). This finding was corroborated

by evidence of increased neuronal packing in overlying neocortex (Figure 9A-9E), including in supragranular layers, which contribute the majority of axon projections that traverse the callosum *en route* to homotopic targets in the contralateral hemisphere (Figure 9D [unpaired two-tailed t-test, $t(4) = 2.9$, $p = 0.04$]). In contrast to these differences in neuronal density, glial density was unchanged (Figure 9F [unpaired two-tailed t-test, $t(4) = 0.64$, $p = 0.56$]), contributing to a statistically insignificant difference in total cell density between groups (Figure 9G [unpaired two-tailed t-test, $t(4) = 1.95$, $p = 0.12$]).

Reductions in axon caliber reflect deficits in nerve conduction in adult *Ube3a*$^{m-/p+}$ mice

What is the functional significance of reduced axon caliber in *Ube3a*$^{m-/p+}$ mice? We sought to answer this question by measuring compound action potential conduction in the sciatic nerve (an easily accessible WM pathway in mice that is amenable to precise measurements of nerve conduction, due to its length). First, we determined whether axon caliber deficits are generalizable to the *Ube3a*$^{m-/p+}$ sciatic nerve. We observed grossly normal myelination, but a significant reduction in mean axon caliber in sciatic nerves of *Ube3a*$^{m-/p+}$ mice compared to control (Figure 10A and 10B [unpaired two-tailed t-test, $t(10) = 2.22$, $p = 0.05$]; Figure 11A, and 11B [unpaired two-tailed t-test, $t(10) = 0.5$, $p = 0.63$]), similar to what we had found in the corpus callosum (Figure 6C). However, relative to callosum (Figures 6F, 7A, and 7B), the caliber of the largest sciatic nerve axons in *Ube3a*$^{m-/p+}$ mice was partially spared (Figure 10C [two-way repeated measures ANOVA for genotype x diameter interaction, $F(14, 140) = 3.33$, $p = 0.0001$]; Figure 11C [two-way repeated measures ANOVA for genotype x diameter interaction, $F(3, 30) = 3.8$, $p = 0.02$; *post hoc* unpaired t-test with Sidak's multiple comparisons correction, $t(40) = 3.6$, $p = 0.003$]), perhaps because many of them arise from motor neurons in

the ventral spinal cord, in which the imprinting of paternal *Ube3a* is relaxed (Huang et al., 2011). Accordingly, the maximum velocity of compound action potentials – a function of nerve conduction though the largest caliber axons – was also spared in *Ube3a*$^{m-/p+}$ sciatic nerves (Figure 10E and 10F [unpaired two-tailed t-test, $t(10) = 0.25$, $p = 0.81$]). Nevertheless, mean compound action potential rise kinetics were significantly slower in *Ube3a*$^{m-/p+}$ sciatic nerves (Figure 10G [unpaired two-tailed t-test, $t(10) = 2.33$, $p = 0.04$]; Figure 10H [unpaired two-tailed t-test, $t(10) = 2.46$, $p = 0.03$]), reflecting the deficit in mean axon caliber (Figure 10B).

DISCUSSION

The present findings indicate that *Ube3a*$^{m-/p+}$ mice closely model the microcephaly observed in AS individuals, and suggest that a major factor contributing to this phenotype is globally impaired WM growth during early postnatal development. Our observations of decreased axon caliber in both the corpus callosum (Figure 6D-6F) and sciatic nerve (Figure 10A-10C) of adult *Ube3a*$^{m-/p+}$ mice lead us to speculate that the radial growth of axons may be especially perturbed by loss of maternal *Ube3a*.

Potential mechanisms underlying axon caliber deficits and microcephaly in *Ube3a*$^{m-/p+}$ mice

The caliber of the largest sciatic nerve axons in *Ube3a*$^{m-/p+}$ mice is relatively preserved (Figure 10C), perhaps reflecting the persistence of paternal *Ube3a* expression in neurons of the ventral spinal cord (Huang et al., 2011). This is consistent with a neuron-specific role for UBE3A in regulating radial axon growth, though we cannot rule out potential effects of UBE3A

haploinsufficiency in myelinating glia, which support radial axon growth subsequent to the initiation of myelination (Sanchez et al., 1996; Tomita et al., 2007; Sherman et al., 2012).

UBE3A interacts with the Armadillo repeat-containing C-terminus of the abnormal spindle-like microcephaly (ASPM) protein (Singhmar and Kumar, 2011), which is encoded by the gene most frequently mutated in cases of autosomal recessive primary microcephaly (Bond et al., 2002; Nicholas et al., 2009). ASPM localizes to the centrosome and midbody where it participates in the positioning of spindle poles and the organization of microtubules into asters, thereby enabling the proper cleavage of symmetrically-dividing neuroepithelial progenitor cells (Fish et al., 2006; Paramasivam et al., 2007; Higgins et al., 2010). Notably, acute shRNA-mediated knock-down of UBE3A in immortalized human kidney cells results in mitotic abnormalities, including disorganized spindles and misseggregated chromosomes (Singhmar and Kumar, 2011). If present in neural stem cell niches in *Ube3a*$^{m-/p+}$ mice or in individuals with AS, these defects could deplete the pool of viable neural progenitors that populate the brain with neurons, leading to microcephaly. However, *Ube3a*$^{m-/p+}$ mice, similar to individuals with AS, do not exhibit microcephaly until the postnatal period, after the completion of neurogenesis and neuronal migration (Figure 1). Presumably, neural stem cells, which bilallelically express *Ube3a* (Judson et al., 2014), express sufficient UBE3A protein from the paternal allele to support normal ASPM function in the event of maternal *Ube3a* loss. ASPM expression wanes in postmitotic neurons (Luers et al., 2002; Kouprina et al., 2005; Williams et al., 2015), whereas the expression of several other Armadillo repeat-containing proteins, including β-catenin, persists. Considering the numerous studies linking β-catenin signaling to axon growth, morphogenesis, and presynaptic function (Bamji et al., 2003; Elul et

al., 2003; David et al., 2008; Pratt et al., 2012; Taylor et al., 2013), potential interactions between UBE3A and β-catenin during early postnatal development merit investigation.

UBE3A has been linked, albeit tentatively (Jensen et al., 2013), to regulation of the actin cytoskeleton, which supports terminal axon branching and the elaboration of developing axonal arbors (Kalil and Dent, 2014). UBE3A is also enriched at nascent presynaptic terminals and plays a role in experience-dependent refinement of synaptic architecture during the early postnatal period (Yashiro et al., 2009; Burette et al., 2016; Kim et al., 2016). Maternal *Ube3a* loss may thus affect the elaboration of axon terminal arbors through distinct mechanisms: directly, by disrupting the actin cytoskeleton during terminal axon branching, and/or indirectly, through deficits in synapse development and stabilization. Because terminal arbor size tends to correlate with the caliber of the parent axon (Stuermer, 1984; Roe et al., 1989; Tsuji and Liberman, 1997; Eatock et al., 2008; Perge et al., 2009), it is possible that reductions in axon caliber in *Ube3a*$^{m-/p+}$ mice are secondary to deficits in terminal axon branching.

The development and maintenance of large axons and their terminal arbors is energetically taxing. Mitochondrial volume fraction in myelinated axons generally scales quadratically to increases in axon caliber and terminal field size, possibly to match energy production to the demands of synaptic transmission within the terminal arbor (Sengupta et al., 2010; Perge et al., 2012). Although we did not find evidence of deficient mitochondrial volume-fraction or morphology in the axons of *Ube3a*$^{m-/p+}$ mice in this or in previous studies (Wallace et al., 2012; Burette et al., 2016; Judson et al., 2016), UBE3A does associate with mitochondrial membranes within neurons of both early postnatal and adult mice, and thus, is poised to regulate mitochondrial function (Burette et al., 2016). This is consistent with recent reports of increased mitochondrial superoxide in the hippocampus of adult *Ube3a*$^{m-/p+}$ mice

(Santini et al., 2015). It will be interesting to determine if mitochondrial dysfunction is more widespread in the brains of young *Ube3a*$^{m-/p+}$ mice, possibly imposing energetic constraints on axon growth.

Abnormal WM morphology in adult *Ube3a*$^{m-/p+}$ mice: relation to neuroimaging findings in AS

Despite marked reductions in axon caliber, we found that the myelination of callosal and sciatic nerve axons was largely intact in adult *Ube3a*$^{m-/p+}$ mice (Figures 6B, 6C, 11A, and 11B). Our DTI tractography study suggests that this is generally true for other tracts in the adult *Ube3a*$^{m-/p+}$ brain as well. RD, often increased in instances of hypomyelination (Song et al., 2002; Song et al., 2005; Harsan et al., 2006; Tyszka et al., 2006), was unchanged in most tracts, or even decreased (Table 2). In contrast, a DTI tractography study of children with AS found RD to be increased in WM tracts throughout the brain (Peters et al., 2011), in agreement with evidence for delayed myelination garnered from a separate T2-weighted MRI study of younger children (Harting et al., 2009). While these seemingly discrepant findings could indicate species differences in UBE3A function, we think it more likely that they highlight the disparate developmental periods explored in our respective studies. We hypothesize that impaired radial axon growth delays the deposition of myelin within both central and peripheral WM tracts in AS – achievement of a minimum axon caliber, presumably delayed in *Ube3a*$^{m-/p+}$ mice, triggers the initiation of myelination by both oligodendrocytes and Schwann cells (Simons and Trotter, 2007; Nave and Trapp, 2008). This would suggest that myelination largely normalizes by adulthood, explaining the findings reported here. To test this hypothesis, future studies in *Ube3a*$^{m-/p+}$ mice should establish the developmental profile of axon caliber deficits in relation

to the course of myelination. Likewise, future AS neuroimaging studies should include adult subjects. Prior neuroimaging studies focused on AS individuals with large deletions of maternal 15q11-q13 (Harting et al., 2009; Peters et al., 2011), which result in the haploinsufficiency of important genes (e.g., $GABA_A$ receptor subunits) in addition to *UBE3A* (Margolis et al., 2015). This facet of the disorder, not modeled by the *Ube3a*$^{m-/p+}$ mouse, could also contribute to the WM pathology associated with maternal *UBE3A* loss in humans.

Functional implications of axon caliber deficits in adult *Ube3a*$^{m-/p+}$ mice

Reduced axon caliber was commensurate with the slowing of compound action potentials in the sciatic nerves of *Ube3a*$^{m-/p+}$ mice (Figure 10). This functional deficit may contribute to the motor dysfunction seen in the model (Jiang et al., 1998; van Woerden et al., 2007; Huang et al., 2013; Mandel-Brehm et al., 2015; Santini et al., 2015). If slowed conduction of action potentials is a property of all WM tracts in *Ube3a*$^{m-/p+}$ mice, this could have a profound brain-wide impact on neural circuit function. For example, slowed conduction could disrupt brain rhythms that provide a temporal framework for grouping and integrating information within and across distributed neural networks; abnormal brain rhythmicity is well-documented in both *Ube3a*$^{m-/p+}$ mice and in individuals with AS (Colas et al., 2005; Thibert et al., 2013; Judson et al., 2016), and may precipitate a range of phenotypes, including cognitive deficits, sleep disturbances, and seizures. Brain rhythms are highly conserved over the course of mammalian evolution, and large-caliber axons have been proposed to enable inter-areal neural synchrony despite tremendous increases in brain scale. Importantly, the bigger the brain, the greater the dependence on rapidly conducting, large-caliber axons (Buzsaki et al.,

2013). Hence, we suggest that decreased axon caliber consequent to loss of UBE3A function may have a far greater functional impact in humans than in mice.

The extent to which axon caliber deficits directly contribute to neural circuit and behavioral dysfunction in *Ube3a*$^{m-/p+}$ mice remains to be determined. Nevertheless, our findings demonstrate that WM abnormalities are a pervasive feature of the adult *Ube3a*$^{m-/p+}$ brain, and these abnormalities are easily detected by standard structural neuroimaging. This also appears to be the case for children with AS (Harting et al., 2009; Peters et al., 2011; Wilson et al., 2011; Tiwari et al., 2012); importantly, the severity of WM microstructural defects in these children may be associated with clinical outcome (Peters et al., 2011). Structural neuroimaging-based studies could further explore the relationship between WM defects and clinical phenotypes in AS, and potentially establish WM volume and integrity as noninvasive biomarkers of both phenotypic progression and response to therapeutic intervention in the disorder.

REFERENCES

Avants BB, Epstein CL, Grossman M, Gee JC (2008) Symmetric diffeomorphic image registration with cross-correlation: evaluating automated labeling of elderly and neurodegenerative brain. Medical image analysis 12:26-41.

Bamji SX, Shimazu K, Kimes N, Huelsken J, Birchmeier W, Lu B, Reichardt LF (2003) Role of beta-catenin in synaptic vesicle localization and presynaptic assembly. Neuron 40:719-731.

Bond J, Roberts E, Mochida GH, Hampshire DJ, Scott S, Askham JM, Springell K, Mahadevan M, Crow YJ, Markham AF, Walsh CA, Woods CG (2002) ASPM is a major determinant of cerebral cortical size. Nature genetics 32:316-320.

Budin F, Hoogstoel M, Reynolds P, Grauer M, O'Leary-Moore SK, Oguz I (2013) Fully automated rodent brain MR image processing pipeline on a Midas server: from acquired images to region-based statistics. Frontiers in neuroinformatics 7:15.

Burette AC, Judson MC, Burette S, Phend KD, Philpot BD, Weinberg RJ (2016) Subcellular organization of UBE3A in neurons. The Journal of comparative neurology.

Buzsaki G, Logothetis N, Singer W (2013) Scaling brain size, keeping timing: evolutionary preservation of brain rhythms. Neuron 80:751-764.

Colas D, Wagstaff J, Fort P, Salvert D, Sarda N (2005) Sleep disturbances in Ube3a maternal-deficient mice modeling Angelman syndrome. Neurobiology of disease 20:471-478.

Cooper EM, Hudson AW, Amos J, Wagstaff J, Howley PM (2004) Biochemical analysis of Angelman syndrome-associated mutations in the E3 ubiquitin ligase E6-associated protein. The Journal of biological chemistry 279:41208-41217.

615 Dagli A, Buiting K, Williams CA (2012) Molecular and Clinical Aspects of Angelman Syndrome.
616 Molecular syndromology 2:100-112.
617 David MD, Yeramian A, Dunach M, Llovera M, Canti C, de Herreros AG, Comella JX, Herreros
618 J (2008) Signalling by neurotrophins and hepatocyte growth factor regulates axon
619 morphogenesis by differential beta-catenin phosphorylation. Journal of cell science
620 121:2718-2730.
621 Eatock RA, Xue J, Kalluri R (2008) Ion channels in mammalian vestibular afferents may set
622 regularity of firing. The Journal of experimental biology 211:1764-1774.
623 El Hokayem J, Nawaz Z (2014) E6AP in the brain: one protein, dual function, multiple
624 diseases. Molecular neurobiology 49:827-839.
625 Elul TM, Kimes NE, Kohwi M, Reichardt LF (2003) N- and C-terminal domains of beta-catenin,
626 respectively, are required to initiate and shape axon arbors of retinal ganglion cells in
627 vivo. The Journal of neuroscience : the official journal of the Society for Neuroscience
628 23:6567-6575.
629 Fish JL, Kosodo Y, Enard W, Paabo S, Huttner WB (2006) Aspm specifically maintains
630 symmetric proliferative divisions of neuroepithelial cells. Proceedings of the National
631 Academy of Sciences of the United States of America 103:10438-10443.
632 Fryburg JS, Breg WR, Lindgren V (1991) Diagnosis of Angelman syndrome in infants.
633 American journal of medical genetics 38:58-64.
634 Goodlett CB, Fletcher PT, Gilmore JH, Gerig G (2009) Group analysis of DTI fiber tract
635 statistics with application to neurodevelopment. NeuroImage 45:S133-142.
636 Harsan LA, Poulet P, Guignard B, Steibel J, Parizel N, de Sousa PL, Boehm N, Grucker D,
637 Ghandour MS (2006) Brain dysmyelination and recovery assessment by noninvasive in

vivo diffusion tensor magnetic resonance imaging. Journal of neuroscience research 83:392-402.

Harting I, Seitz A, Rating D, Sartor K, Zschocke J, Janssen B, Ebinger F, Wolf NI (2009) Abnormal myelination in Angelman syndrome. European journal of paediatric neurology : EJPN : official journal of the European Paediatric Neurology Society 13:271-276.

Higgins J, Midgley C, Bergh AM, Bell SM, Askham JM, Roberts E, Binns RK, Sharif SM, Bennett C, Glover DM, Woods CG, Morrison EE, Bond J (2010) Human ASPM participates in spindle organisation, spindle orientation and cytokinesis. BMC cell biology 11:85.

Huang HS, Burns AJ, Nonneman RJ, Baker LK, Riddick NV, Nikolova VD, Riday TT, Yashiro K, Philpot BD, Moy SS (2013) Behavioral deficits in an Angelman syndrome model: effects of genetic background and age. Behavioural brain research 243:79-90.

Huang HS, Allen JA, Mabb AM, King IF, Miriyala J, Taylor-Blake B, Sciaky N, Dutton JW, Jr., Lee HM, Chen X, Jin J, Bridges AS, Zylka MJ, Roth BL, Philpot BD (2011) Topoisomerase inhibitors unsilence the dormant allele of Ube3a in neurons. Nature 481:185-189.

Jensen L, Farook MF, Reiter LT (2013) Proteomic profiling in Drosophila reveals potential Dube3a regulation of the actin cytoskeleton and neuronal homeostasis. PloS one 8:e61952.

Jiang YH, Armstrong D, Albrecht U, Atkins CM, Noebels JL, Eichele G, Sweatt JD, Beaudet AL (1998) Mutation of the Angelman ubiquitin ligase in mice causes increased cytoplasmic p53 and deficits of contextual learning and long-term potentiation. Neuron 21:799-811.

660 Joshi S, Davis B, Jomier M, Gerig G (2004) Unbiased diffeomorphic atlas construction for
661 computational anatomy. NeuroImage 23 Suppl 1:S151-160.
662 Judson MC, Sosa-Pagan JO, Del Cid WA, Han JE, Philpot BD (2014) Allelic specificity of
663 Ube3a expression in the mouse brain during postnatal development. The Journal of
664 comparative neurology 522:1874-1896.
665 Judson MC, Wallace ML, Sidorov MS, Burette AC, Gu B, van Woerden GM, King IF, Han JE,
666 Zylka MJ, Elgersma Y, Weinberg RJ, Philpot BD (2016) GABAergic Neuron-Specific
667 Loss of Ube3a Causes Angelman Syndrome-Like EEG Abnormalities and Enhances
668 Seizure Susceptibility. Neuron 90:56-69.
669 Kalil K, Dent EW (2014) Branch management: mechanisms of axon branching in the
670 developing vertebrate CNS. Nature reviews Neuroscience 15:7-18.
671 Kim H, Kunz PA, Mooney R, Philpot BD, Smith SL (2016) Maternal Loss of Ube3a Impairs
672 Experience-Driven Dendritic Spine Maintenance in the Developing Visual Cortex. The
673 Journal of neuroscience : the official journal of the Society for Neuroscience 36:4888-
674 4894.
675 Kishino T, Lalande M, Wagstaff J (1997) UBE3A/E6-AP mutations cause Angelman syndrome.
676 Nature genetics 15:70-73.
677 Kouprina N, Pavlicek A, Collins NK, Nakano M, Noskov VN, Ohzeki J, Mochida GH, Risinger
678 JI, Goldsmith P, Gunsior M, Solomon G, Gersch W, Kim JH, Barrett JC, Walsh CA,
679 Jurka J, Masumoto H, Larionov V (2005) The microcephaly ASPM gene is expressed in
680 proliferating tissues and encodes for a mitotic spindle protein. Human molecular
681 genetics 14:2155-2165.

682 Luers GH, Michels M, Schwaab U, Franz T (2002) Murine calmodulin binding protein 1
683 (Calmbp1): tissue-specific expression during development and in adult tissues.
684 Mechanisms of development 118:229-232.
685 Ma Y, Hof PR, Grant SC, Blackband SJ, Bennett R, Slatest L, McGuigan MD, Benveniste H
686 (2005) A three-dimensional digital atlas database of the adult C57BL/6J mouse brain by
687 magnetic resonance microscopy. Neuroscience 135:1203-1215.
688 Mabb AM, Ehlers MD (2010) Ubiquitination in postsynaptic function and plasticity. Annual
689 review of cell and developmental biology 26:179-210.
690 Mabb AM, Judson MC, Zylka MJ, Philpot BD (2011) Angelman syndrome: insights into
691 genomic imprinting and neurodevelopmental phenotypes. Trends in neurosciences
692 34:293-303.
693 Madisen L, Zwingman TA, Sunkin SM, Oh SW, Zariwala HA, Gu H, Ng LL, Palmiter RD,
694 Hawrylycz MJ, Jones AR, Lein ES, Zeng H (2010) A robust and high-throughput Cre
695 reporting and characterization system for the whole mouse brain. Nature neuroscience
696 13:133-140.
697 Mandel-Brehm C, Salogiannis J, Dhamne SC, Rotenberg A, Greenberg ME (2015) Seizure-
698 like activity in a juvenile Angelman syndrome mouse model is attenuated by reducing
699 Arc expression. Proceedings of the National Academy of Sciences of the United States
700 of America 112:5129-5134.
701 Margolis SS, Sell GL, Zbinden MA, Bird LM (2015) Angelman Syndrome. Neurotherapeutics :
702 the journal of the American Society for Experimental NeuroTherapeutics 12:641-650.

703 Matsuura T, Sutcliffe JS, Fang P, Galjaard RJ, Jiang YH, Benton CS, Rommens JM, Beaudet
704 AL (1997) De novo truncating mutations in E6-AP ubiquitin-protein ligase gene (UBE3A)
705 in Angelman syndrome. Nature genetics 15:74-77.
706 Mori S, Zhang J (2006) Principles of diffusion tensor imaging and its applications to basic
707 neuroscience research. Neuron 51:527-539.
708 Mulherkar SA, Jana NR (2010) Loss of dopaminergic neurons and resulting behavioural
709 deficits in mouse model of Angelman syndrome. Neurobiology of disease 40:586-592.
710 Nave KA, Trapp BD (2008) Axon-glial signaling and the glial support of axon function. Annual
711 review of neuroscience 31:535-561.
712 Nawaz Z, Lonard DM, Smith CL, Lev-Lehman E, Tsai SY, Tsai MJ, O'Malley BW (1999) The
713 Angelman syndrome-associated protein, E6-AP, is a coactivator for the nuclear
714 hormone receptor superfamily. Molecular and cellular biology 19:1182-1189.
715 Nicholas AK, Swanson EA, Cox JJ, Karbani G, Malik S, Springell K, Hampshire D, Ahmed M,
716 Bond J, Di Benedetto D, Fichera M, Romano C, Dobyns WB, Woods CG (2009) The
717 molecular landscape of ASPM mutations in primary microcephaly. Journal of medical
718 genetics 46:249-253.
719 Paramasivam M, Chang YJ, LoTurco JJ (2007) ASPM and citron kinase co-localize to the
720 midbody ring during cytokinesis. Cell cycle 6:1605-1612.
721 Perge JA, Koch K, Miller R, Sterling P, Balasubramanian V (2009) How the optic nerve
722 allocates space, energy capacity, and information. The Journal of neuroscience : the
723 official journal of the Society for Neuroscience 29:7917-7928.

724 Perge JA, Niven JE, Mugnaini E, Balasubramanian V, Sterling P (2012) Why do axons differ in
725 caliber? The Journal of neuroscience : the official journal of the Society for
726 Neuroscience 32:626-638.
727 Peters SU, Kaufmann WE, Bacino CA, Anderson AW, Adapa P, Chu Z, Yallampalli R, Traipe
728 E, Hunter JV, Wilde EA (2011) Alterations in white matter pathways in Angelman
729 syndrome. Developmental medicine and child neurology 53:361-367.
730 Pillai AM, Thaxton C, Pribisko AL, Cheng JG, Dupree JL, Bhat MA (2009) Spatiotemporal
731 ablation of myelinating glia-specific neurofascin (Nfasc NF155) in mice reveals gradual
732 loss of paranodal axoglial junctions and concomitant disorganization of axonal domains.
733 Journal of neuroscience research 87:1773-1793.
734 Pratt T, Davey JW, Nowakowski TJ, Raasumaa C, Rawlik K, McBride D, Clinton M, Mason JO,
735 Price DJ (2012) The expression and activity of beta-catenin in the thalamus and its
736 projections to the cerebral cortex in the mouse embryo. BMC neuroscience 13:20.
737 Reid G, Hubner MR, Metivier R, Brand H, Denger S, Manu D, Beaudouin J, Ellenberg J,
738 Gannon F (2003) Cyclic, proteasome-mediated turnover of unliganded and liganded
739 ERalpha on responsive promoters is an integral feature of estrogen signaling. Molecular
740 cell 11:695-707.
741 Roe AW, Garraghty PE, Sur M (1989) Terminal arbors of single ON-center and OFF-center X
742 and Y retinal ganglion cell axons within the ferret's lateral geniculate nucleus. The
743 Journal of comparative neurology 288:208-242.
744 Rougeulle C, Glatt H, Lalande M (1997) The Angelman syndrome candidate gene, UBE3A/E6-
745 AP, is imprinted in brain. Nature genetics 17:14-15.

746 Sanchez I, Hassinger L, Paskevich PA, Shine HD, Nixon RA (1996) Oligodendroglia regulate
747 the regional expansion of axon caliber and local accumulation of neurofilaments during
748 development independently of myelin formation. The Journal of neuroscience : the
749 official journal of the Society for Neuroscience 16:5095-5105.
750 Santini E, Turner KL, Ramaraj AB, Murphy MP, Klann E, Kaphzan H (2015) Mitochondrial
751 Superoxide Contributes to Hippocampal Synaptic Dysfunction and Memory Deficits in
752 Angelman Syndrome Model Mice. The Journal of neuroscience : the official journal of
753 the Society for Neuroscience 35:16213-16220.
754 Schneider CA, Rasband WS, Eliceiri KW (2012) NIH Image to ImageJ: 25 years of image
755 analysis. Nature methods 9:671-675.
756 Sell GL, Margolis SS (2015) From UBE3A to Angelman syndrome: a substrate perspective.
757 Frontiers in neuroscience 9:322.
758 Sengupta B, Stemmler M, Laughlin SB, Niven JE (2010) Action potential energy efficiency
759 varies among neuron types in vertebrates and invertebrates. PLoS computational
760 biology 6:e1000840.
761 Sherman DL, Krols M, Wu LM, Grove M, Nave KA, Gangloff YG, Brophy PJ (2012) Arrest of
762 myelination and reduced axon growth when Schwann cells lack mTOR. The Journal of
763 neuroscience : the official journal of the Society for Neuroscience 32:1817-1825.
764 Simons M, Trotter J (2007) Wrapping it up: the cell biology of myelination. Current opinion in
765 neurobiology 17:533-540.
766 Singhmar P, Kumar A (2011) Angelman syndrome protein UBE3A interacts with primary
767 microcephaly protein ASPM, localizes to centrosomes and regulates chromosome
768 segregation. PloS one 6:e20397.

769 Song SK, Sun SW, Ramsbottom MJ, Chang C, Russell J, Cross AH (2002) Dysmyelination
770 revealed through MRI as increased radial (but unchanged axial) diffusion of water.
771 NeuroImage 17:1429-1436.
772 Song SK, Yoshino J, Le TQ, Lin SJ, Sun SW, Cross AH, Armstrong RC (2005) Demyelination
773 increases radial diffusivity in corpus callosum of mouse brain. NeuroImage 26:132-140.
774 Stuermer CA (1984) Rules for retinotectal terminal arborizations in the goldfish optic tectum: a
775 whole-mount study. The Journal of comparative neurology 229:214-232.
776 Sutcliffe JS, Jiang YH, Galijaard RJ, Matsuura T, Fang P, Kubota T, Christian SL, Bressler J,
777 Cattanach B, Ledbetter DH, Beaudet AL (1997) The E6-Ap ubiquitin-protein ligase
778 (UBE3A) gene is localized within a narrowed Angelman syndrome critical region.
779 Genome research 7:368-377.
780 Taylor AM, Wu J, Tai HC, Schuman EM (2013) Axonal translation of beta-catenin regulates
781 synaptic vesicle dynamics. The Journal of neuroscience : the official journal of the
782 Society for Neuroscience 33:5584-5589.
783 Thibert RL, Larson AM, Hsieh DT, Raby AR, Thiele EA (2013) Neurologic manifestations of
784 Angelman syndrome. Pediatric neurology 48:271-279.
785 Tiwari VN, Jeong JW, Wilson BJ, Behen ME, Chugani HT, Sundaram SK (2012) Relationship
786 between aberrant brain connectivity and clinical features in Angelman Syndrome: a new
787 method using tract based spatial statistics of DTI color-coded orientation maps.
788 NeuroImage 59:349-355.
789 Tomita K, Kubo T, Matsuda K, Fujiwara T, Yano K, Winograd JM, Tohyama M, Hosokawa K
790 (2007) The neurotrophin receptor p75NTR in Schwann cells is implicated in
791 remyelination and motor recovery after peripheral nerve injury. Glia 55:1199-1208.

792 Tsuji J, Liberman MC (1997) Intracellular labeling of auditory nerve fibers in guinea pig: central
793 and peripheral projections. The Journal of comparative neurology 381:188-202.
794 Tyszka JM, Readhead C, Bearer EL, Pautler RG, Jacobs RE (2006) Statistical diffusion tensor
795 histology reveals regional dysmyelination effects in the shiverer mouse mutant.
796 NeuroImage 29:1058-1065.
797 van Woerden GM, Harris KD, Hojjati MR, Gustin RM, Qiu S, de Avila Freire R, Jiang YH,
798 Elgersma Y, Weeber EJ (2007) Rescue of neurological deficits in a mouse model for
799 Angelman syndrome by reduction of alphaCaMKII inhibitory phosphorylation. Nature
800 neuroscience 10:280-282.
801 Verde AR, Budin F, Berger JB, Gupta A, Farzinfar M, Kaiser A, Ahn M, Johnson H, Matsui J,
802 Hazlett HC, Sharma A, Goodlett C, Shi Y, Gouttard S, Vachet C, Piven J, Zhu H, Gerig
803 G, Styner M (2014) UNC-Utah NA-MIC framework for DTI fiber tract analysis. Frontiers
804 in neuroinformatics 7:51.
805 Wallace ML, Burette AC, Weinberg RJ, Philpot BD (2012) Maternal loss of Ube3a produces an
806 excitatory/inhibitory imbalance through neuron type-specific synaptic defects. Neuron
807 74:793-800.
808 Williams SE, Garcia I, Crowther AJ, Li S, Stewart A, Liu H, Lough KJ, O'Neill S, Veleta K,
809 Oyarzabal EA, Merrill JR, Shih YY, Gershon TR (2015) Aspm sustains postnatal
810 cerebellar neurogenesis and medulloblastoma growth in mice. Development 142:3921-
811 3932.
812 Wilson BJ, Sundaram SK, Huq AH, Jeong JW, Halverson SR, Behen ME, Bui DQ, Chugani HT
813 (2011) Abnormal language pathway in children with Angelman syndrome. Pediatric
814 neurology 44:350-356.

Yamasaki K, Joh K, Ohta T, Masuzaki H, Ishimaru T, Mukai T, Niikawa N, Ogawa M, Wagstaff J, Kishino T (2003) Neurons but not glial cells show reciprocal imprinting of sense and antisense transcripts of Ube3a. Human molecular genetics 12:837-847.

Yashiro K, Riday TT, Condon KH, Roberts AC, Bernardo DR, Prakash R, Weinberg RJ, Ehlers MD, Philpot BD (2009) Ube3a is required for experience-dependent maturation of the neocortex. Nature neuroscience 12:777-783.

Yushkevich PA, Piven J, Hazlett HC, Smith RG, Ho S, Gee JC, Gerig G (2006) User-guided 3D active contour segmentation of anatomical structures: significantly improved efficiency and reliability. NeuroImage 31:1116-1128.

Zhu H, Kong L, Li R, Styner M, Gerig G, Lin W, Gilmore JH (2011) FADTTS: functional analysis of diffusion tensor tract statistics. NeuroImage 56:1412-1425.

FIGURE LEGENDS

Figure 1. *Ube3a*$^{m-/p+}$ mice exhibit microcephaly with postnatal onset.

(**A**) Representative image of P28 *Ube3a*$^{m+/p+}$ and *Ube3a*$^{m-/p+}$ littermate brains following transcardial fixation and gross dissection. (**B**) Cross-sectional analysis of post-perfusion brain weight from littermate *Ube3a*$^{m+/p+}$ and *Ube3a*$^{m-/p+}$ mice. (**C**) Cross-sectional analysis of premortem body weight from littermate *Ube3a*$^{m+/p+}$ and *Ube3a*$^{m-/p+}$ mice (P0: *Ube3a*$^{m+/p+}$ n = 7, *Ube3a*$^{m-/p+}$ n = 6; P6: *Ube3a*$^{m+/p+}$ n = 6, *Ube3a*$^{m-/p+}$ n = 13; P7: *Ube3a*$^{m+/p+}$ n = 8, *Ube3a*$^{m-/p+}$ n = 11; P8: *Ube3a*$^{m+/p+}$ n = 10, *Ube3a*$^{m-/p+}$ n = 7; P14: *Ube3a*$^{m+/p+}$ n = 8, *Ube3a*$^{m-/p+}$ n = 6; P16: *Ube3a*$^{m+/p+}$ n = 7, *Ube3a*$^{m-/p+}$ n = 10; P28: *Ube3a*$^{m+/p+}$ n = 7, *Ube3a*$^{m-/p+}$ n = 5; P90: *Ube3a*$^{m+/p+}$ n = 5, *Ube3a*$^{m-/p+}$ n = 6). Each data set was fit with a single exponential. Data represent mean ± SEM. ***p≤0.001, ****p≤0.0001.

Figure 2. Cortical patterning is normal in adult *Ube3a*$^{m-/p+}$ mice.

(**A**) Images of DAPI-counterstained tangential cortical sections from ~P90 wildtype (*Scnn1a-Cre::Ai9::Ube3a*$^{m+/p+}$) and *Ube3a*$^{m-/p+}$ (*Scnn1a-Cre::Ai9::Ube3a*$^{m-/p+}$) littermate mice expressing tdTomato in sensory cortices under the control of a L4-specific Cre driver. Scale bar = 1.8 mm. (**B**) Representative sensory maps from *Ube3a*$^{m+/p+}$ and *Ube3a*$^{m-/p+}$ mice. (**C**) Quantification of primary somatosensory (S1), visual (V1), and auditory (A1) cortical surface area as a percentage of total sensory cortical surface area (*Ube3a*$^{m+/p+}$ n = 5 mice, *Ube3a*$^{m-/p+}$ n = 3 mice). (**D** and **E**) Immunostaining for the L2-4 marker CUX1 and the L5-6 marker CTIP2 with DAPI nuclear counterstaining in primary somatosensory cortex of ~P90 *Ube3a*$^{m+/p+}$ (D) and *Ube3a*$^{m-/p+}$ (E) mice. Scale bar = 185 μm. (**F**) Quantification of laminar contributions to

cortical thickness (*Ube3a*$^{m+/p+}$ n = 3 mice, *Ube3a*$^{m-/p+}$ n = 3 mice). Data represent mean ± SEM.

Figure 3. Corpus callosum and internal capsule volumes are disproportionately reduced in adult *Ube3a*$^{m-/p+}$ mice.

(**A** and **B**) Representative three-dimensional (3D) volumetric renderings of cerebral cortex (magenta), corpus callosum (green), and internal capsule (cyan) from *Ube3a*$^{m+/p+}$ (A) and *Ube3a*$^{m-/p+}$ (B) mice. Insets illustrate color-coded segmentation labels in register with (left to right) horizontal, coronal, and sagittal RD image slices, which reflect the plane of view for corresponding 3D renderings (indicated by arrows). (**C**) MRI-based quantification of total cerebral cortical volume, excluding underlying WM. (**D** and **E**) Quantification of corpus callosum (D) and internal capsule (E) volume as a ratio of total cerebral cortical volume (*Ube3a*$^{m+/p+}$ n = 7 mice, *Ube3a*$^{m-/p+}$ n = 5 mice). Data represent mean ± SEM. *p≤0.05, **p≤0.01.

Figure 4. Decreased ratios of WM volume to whole brain and forebrain volumes in adult *Ube3a*$^{m-/p+}$ mice.

(**A**-**E**) Quantification of corpus callosum (A), internal capsule (B), anterior commissure (C), fornix (D), and fimbria (E) volumes as a ratio of both whole brain volume and forebrain volume in *Ube3a*$^{m+/p+}$ (n = 7) and *Ube3a*$^{m-/p+}$ (n = 5) mice). Data represent mean ± SEM. *p≤0.05, **p≤0.01, ***p≤0.001, ****p≤0.0001.

Figure 5. DTI tractography reveals deficits in callosal WM integrity in adult *Ube3a*$^{m-/p+}$ mice.

(**A-C**) Tractography-computed callosal tract (713 fibers) in register with coronal and sagittal views of the FA atlas, which was generated from the average DTI of all *Ube3a*$^{m+/p+}$ (n = 7) and *Ube3a*$^{m-/p+}$ (n = 6) mice. The isthmus of the callosum was not computed. Dorsal (A) and lateral views – from right (B), from left (C) –are shown. Color scale corresponds to arc-length position for statistical sampling along the mediolateral aspect of the tract. (**D**) Distribution of false discovery rate-corrected local p-values (-log10) for each diffusion parameter along the arc-length of the callosal tract. Dashed line indicates p=0.05 significance threshold. (**E**) Tract-based statistical summaries for each diffusion measure: axial diffusivity (AD), radial diffusivity (RD), mean diffusivity (MD), and fractional anisotropy (FA). Y-axis values for AD, RD, and MD are multiplied by 10^3. Data represent mean ± SEM.

Figure 6. Callosal axons in adult *Ube3a*$^{m-/p+}$ mice display normal myelination but decreased caliber.

(**A**) Representative electron micrographs used to assess axon g-ratio in ~P90 *Ube3a*$^{m+/p+}$ and *Ube3a*$^{m-/p+}$ mice. Scale bar = 0.18 μm. (**B**) Quantification of mean axon g-ratio. (**C**) Plots of axon g-ratio versus diameter, fit with a linear function. (**D**) Representative electron micrographic montages of the corpus callosum used to measure the cross-sectional area and packing density of myelinated axons in ~P90 *Ube3a*$^{m+/p+}$ and *Ube3a*$^{m-/p+}$ mice. Scale bar = 2 μm. (**E**) Quantification of the cross-sectional area of myelinated axons. (**F**) Distribution of the diameters of myelinated axons (logarithmic scale). (**G**) Quantification of total axon density. N

= 6 mice for each genotypic group. Data represent mean ± SEM. *p≤0.05, **p≤0.01, ***p≤0.001, ****p≤0.0001.

Figure 7. Myelinated callosal axon diameter (linear scale).

(**A** and **B**) Histograms of myelinated callosal axons analyzed in g-ratio (A, replotting of Figure 6C diameter data) and axon caliber analyses (B, replotting of Figure 6F diameter data). Left panels indicate the percentage of axons distributed among bins of the given diameter ranges. Right panels display the same data normalized to wildtype (*Ube3a*$^{m+/p+}$) values. N = 6 mice for each genotypic group. Data represent mean ± SEM. *p≤0.05, **p≤0.01, ***p≤0.001, ****p≤0.0001.

Figure 8. Analysis of unmyelinated callosal axon caliber in adult *Ube3a*$^{m-/p+}$ mice.

(**A**) Quantification of the cross-sectional area of unmyelinated axons. (**B**) Distribution of the diameters of unmyelinated axons (logarithmic scale). (**C**) Left panel indicates the percentage of unmyelinated axons in the corpus callosum distributed among bins of the given diameter ranges. Right panel displays the same data normalized to wildtype (*Ube3a*$^{m+/p+}$) values. N = 6 mice for each genotypic group. Data represent mean ± SEM.

Figure 9. Packing density of cortical neurons is increased in adult *Ube3a*$^{m-/p+}$ mice.

(**A** and **B**) Immunostaining for the neuronal marker, NEUN, with DAPI nuclear counterstaining in primary somatosensory cortex of ~P90 *Ube3a*$^{m+/p+}$ (A) and *Ube3a*$^{m-/p+}$ (B) mice. Scale bars = 200 μm for far-left panels, 175 μm for representative counting strips, and 18 μm for zoomed images of L5 and L2/3. (**C**-**G**) Quantification of total neuronal density (C), L1-4 neuronal

density (D), L5-6 neuronal density (E), glial density (F), and total cell density (G). N = 3 mice for each genotypic group. Data represent mean ± SEM. *p≤0.05.

Figure 10. Reduced axon caliber correlates with deficits in sciatic nerve conduction in adult *Ube3a*$^{m-/p+}$ mice.

(**A**) Representative electron micrographs of the sciatic nerve from ~P90 *Ube3a*$^{m+/p+}$ and *Ube3a*$^{m-/p+}$ mice. Scale bar = 6.4 μm. (**B**) Quantification of the cross-sectional area of myelinated axons. (**C**) Distribution of the diameters of myelinated axons (logarithmic scale). (**D**) Schematic for *ex vivo* recording of sciatic nerve conduction. (**E**) Averaged compound action potential for each genotypic group (amplitude-normalized). Dashed lines indicate peak of averaged compound action potentials. Scale bars = 1 ms and 100 μs (inset). (**F**-**H**) Quantification of conduction velocity (F), rise time (G), and rise slope (H) for compound action potentials conducted by myelinated Aαβ fibers. N = 6 mice for each genotypic group. Data represent mean ± SEM. *p≤0.05, **p≤0.001, ****p≤0.001.

Figure 11. Analysis of g-ratio and diameter (linear scale) of myelinated axons in the sciatic nerve of adult *Ube3a*$^{m-/p+}$ mice.

(**A**) Quantification of mean axon g-ratio. (**B**) Plots of axon g-ratio versus diameter, fit with a linear function. (**C**) Axon diameter histograms, linear scale (replotting of Figure 10C diameter data). Left panels indicate the percentage of axons distributed among bins of the given diameter ranges. Right panels display the same data normalized to wildtype (*Ube3a*$^{m+/p+}$) values. N = 6 mice for each genotypic group. Data represent mean ± SEM. **p≤0.01.

ILLUSTRATIONS AND TABLES

Table 1. Group comparisons of white matter volume (mm^3).

	Ube3a$^{m+/p+}$		*Ube3a*$^{m-/p+}$			[a]MANCOVA		
	EMM	SEM	EMM	SEM	% Difference	F	p-value	Partial η^2
corpus callosum	0.29	0.005	0.25	0.006	-13.5 ± 0.9	24.2	***0.00061***	0.708
internal capsule	3.15	0.035	2.73	0.038	-13.4 ± 1.0	69.3	***0.00001***	0.874
anterior commissure	0.68	0.014	0.59	0.016	-13.44 ± 1.7	19.4	***0.00134***	0.659
fornix	0.67	0.018	0.59	0.020	-11.34 ± 2.9	8.2	***0.0169***	0.452
fimbria	1.77	0.041	1.56	0.044	-11.39 ± 2.1	11.8	***0.00639***	0.541

[a]Post hoc testing of genotype effects for each tract following MANCOVA (Pillai's Trace, $p<0.005$; genotype as the fixed factor, imaging cohort as the covariate); EMM, Estimated Marginal Mean; SEM, Standard Error of the Mean. *Ube3a*$^{m+/p+}$ N = 7; *Ube3a*$^{m-/p+}$ N = 6.

Table 2. Group comparisons of anisotropy and diffusivity.

		Ube3a$^{m+/p+}$		*Ube3a*$^{m-/p+}$		
		Mean	SEM	Mean	SEM	[a]p-value
corpus callosum	AD	0.62	0.023	0.54	0.019	***≤ 0.001***
	RD	0.16	0.005	0.16	0.004	0.834
	MD	0.31	0.011	0.28	0.009	***0.005***
	FA	0.71	0.006	0.65	0.007	***≤ 0.001***
internal capsule	AD	0.54	0.008	0.51	0.009	***≤ 0.001***
	RD	0.22	0.005	0.22	0.005	0.198
	MD	0.33	0.006	0.31	0.006	***0.009***
	FA	0.53	0.004	0.52	0.006	0.21
anterior commissure	AD	0.62	0.019	0.59	0.019	***0.004***
	RD	0.18	0.003	0.18	0.002	0.416
	MD	0.32	0.008	0.31	0.007	***0.011***
	FA	0.65	0.004	0.65	0.008	0.056
precommissural fornix	AD	0.61	0.009	0.6	0.01	0.066
	RD	0.24	0.004	0.23	0.005	***0.013***
	MD	0.36	0.005	0.35	0.006	***0.011***
	FA	0.55	0.006	0.55	0.006	0.611
postcommissural fornix	AD	0.66	0.02	0.62	0.021	***0.002***
	RD	0.29	0.011	0.27	0.012	***0.013***
	MD	0.42	0.014	0.39	0.015	***0.007***
	FA	0.5	0.005	0.5	0.005	0.144
fimbria	AD	0.81	0.05	0.73	0.033	***0.002***
	RD	0.2	0.013	0.18	0.009	***0.01***
	MD	0.41	0.025	0.37	0.017	***0.003***
	FA	0.73	0.007	0.73	0.003	0.794

[a]Post hoc testing of genotype effects using Functional Analysis of Diffusion Tensor Tracts Statistics (FADDTS) (Zhu et al., 2011). Imaging cohort was set as the covariate. Global p-values are indicated. SEM, Standard Error of the Mean; AD, axial diffusivity; RD, radial diffusivity; MD, mean diffusivity; FA, fractional anisotropy. Values for AD, RD, and MD are multiplied by 10^3. *Ube3a*$^{m+/p+}$ N = 7; *Ube3a*$^{m-/p+}$ N = 6.

Figure 1. *Ube3a*$^{m-/p+}$ mice exhibit microcephaly with postnatal onset.

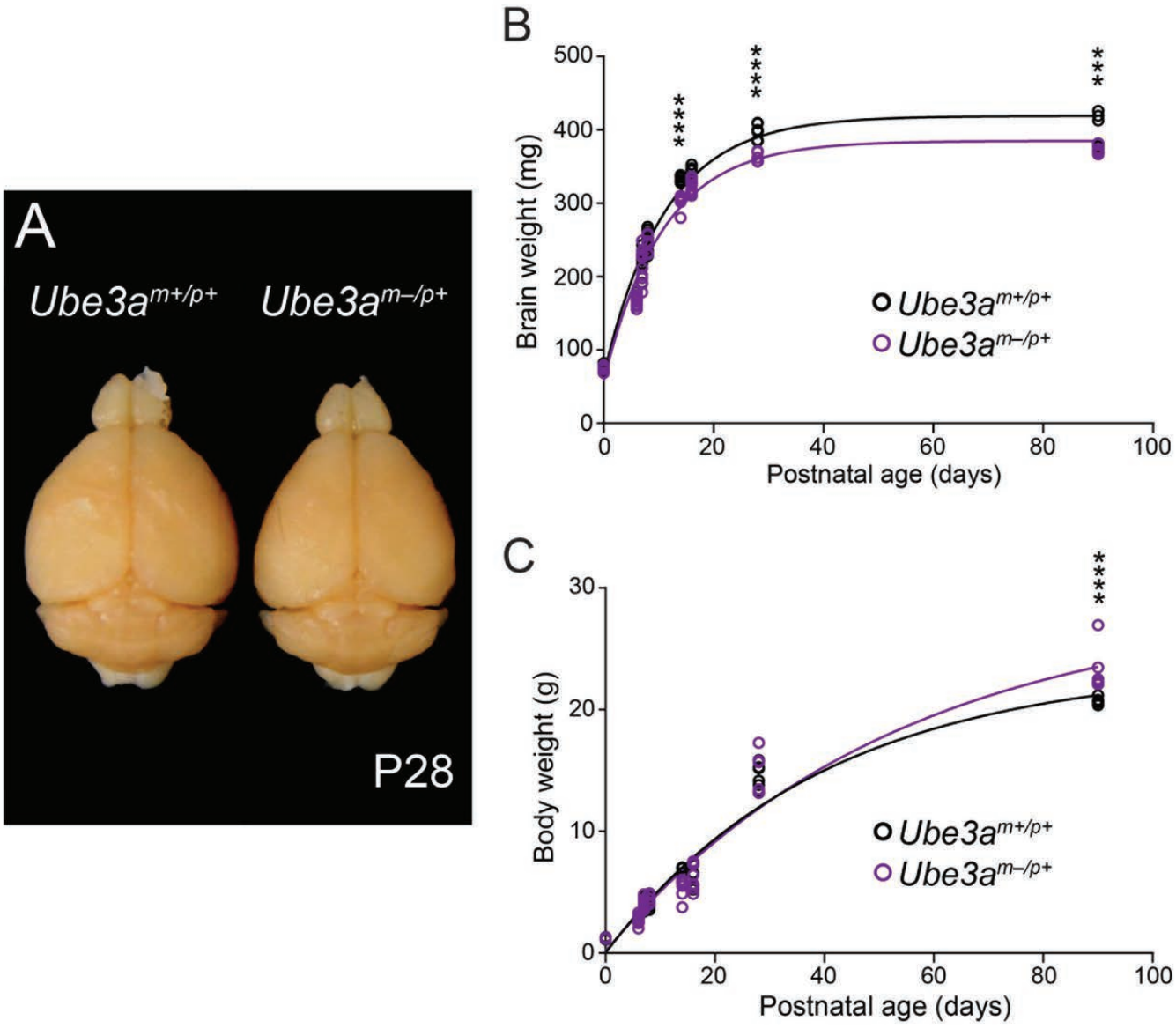

Figure 2. Cortical patterning is normal in *Ube3a*$^{m-/p+}$ mice.

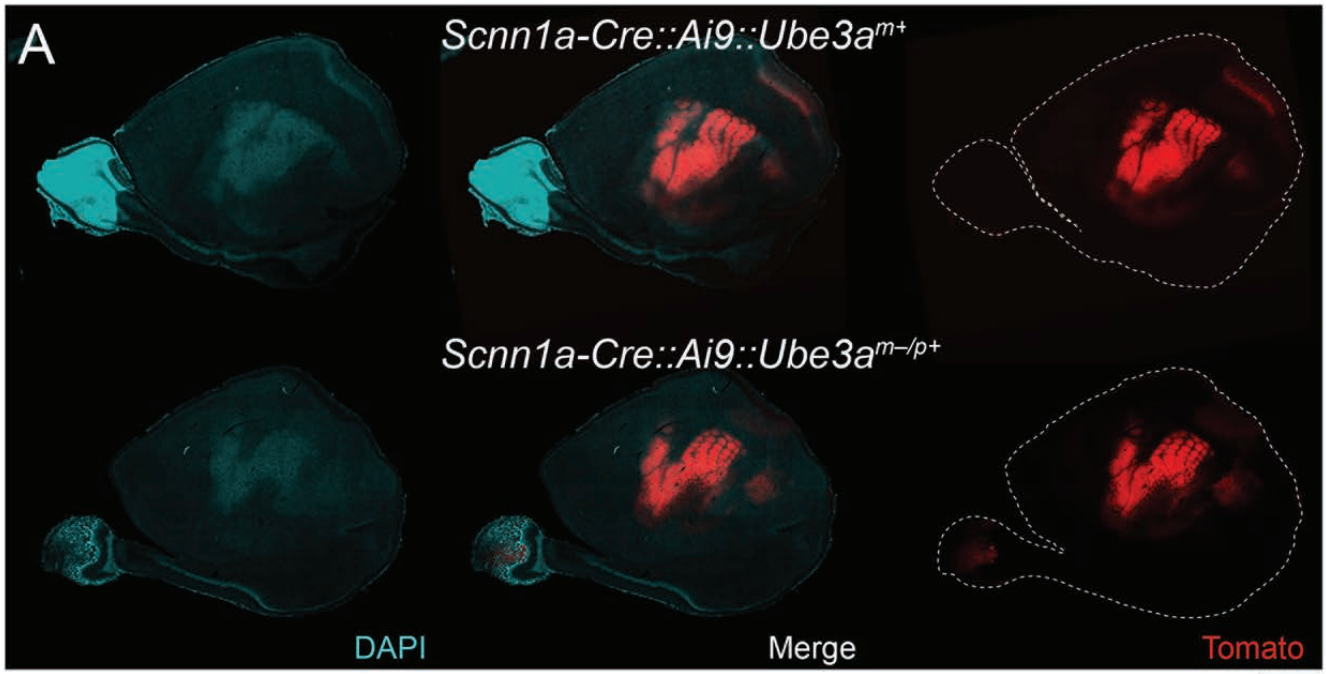

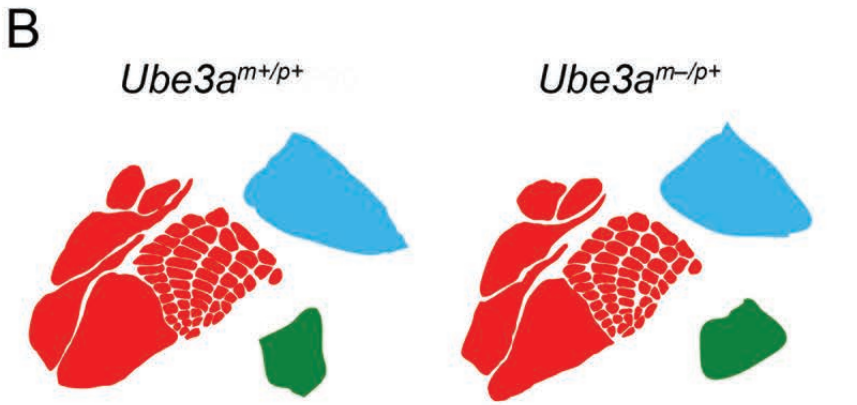

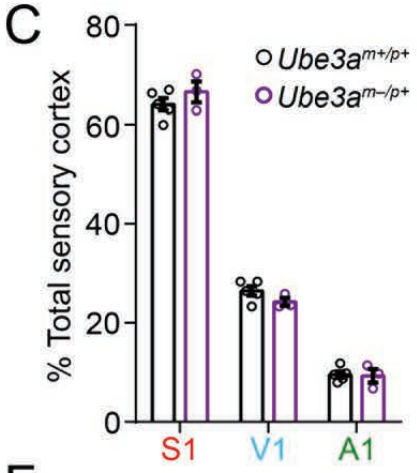

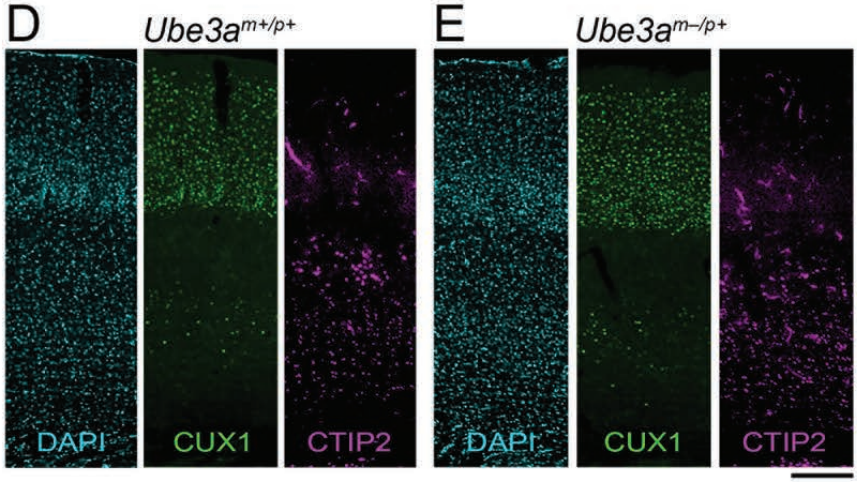

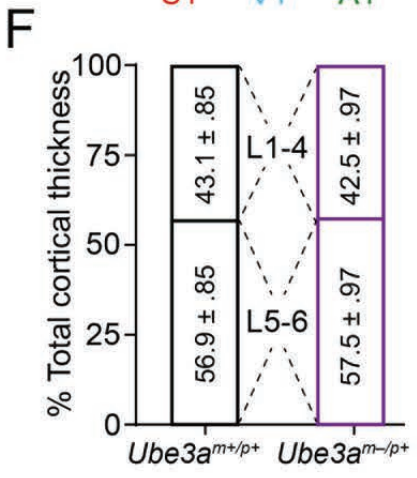

Figure 3. Corpus callosum and internal capsule volumes are disproportionately reduced in *Ube3a*$^{m-/p+}$ mice.

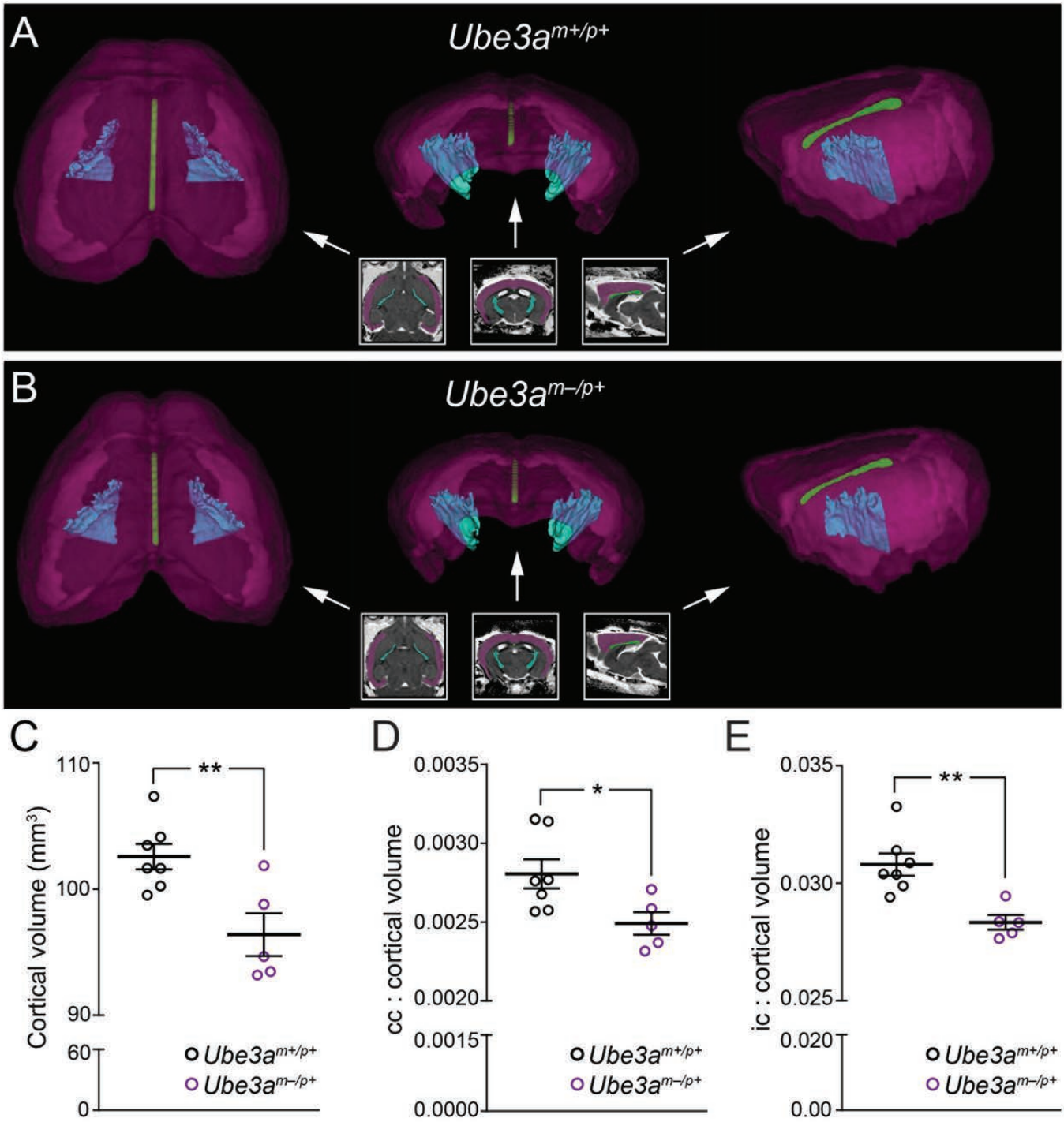

Figure 4. Decreased ratios of WM volume to whole brain and forebrain volumes in adult *Ube3a*$^{m-/p+}$ mice.

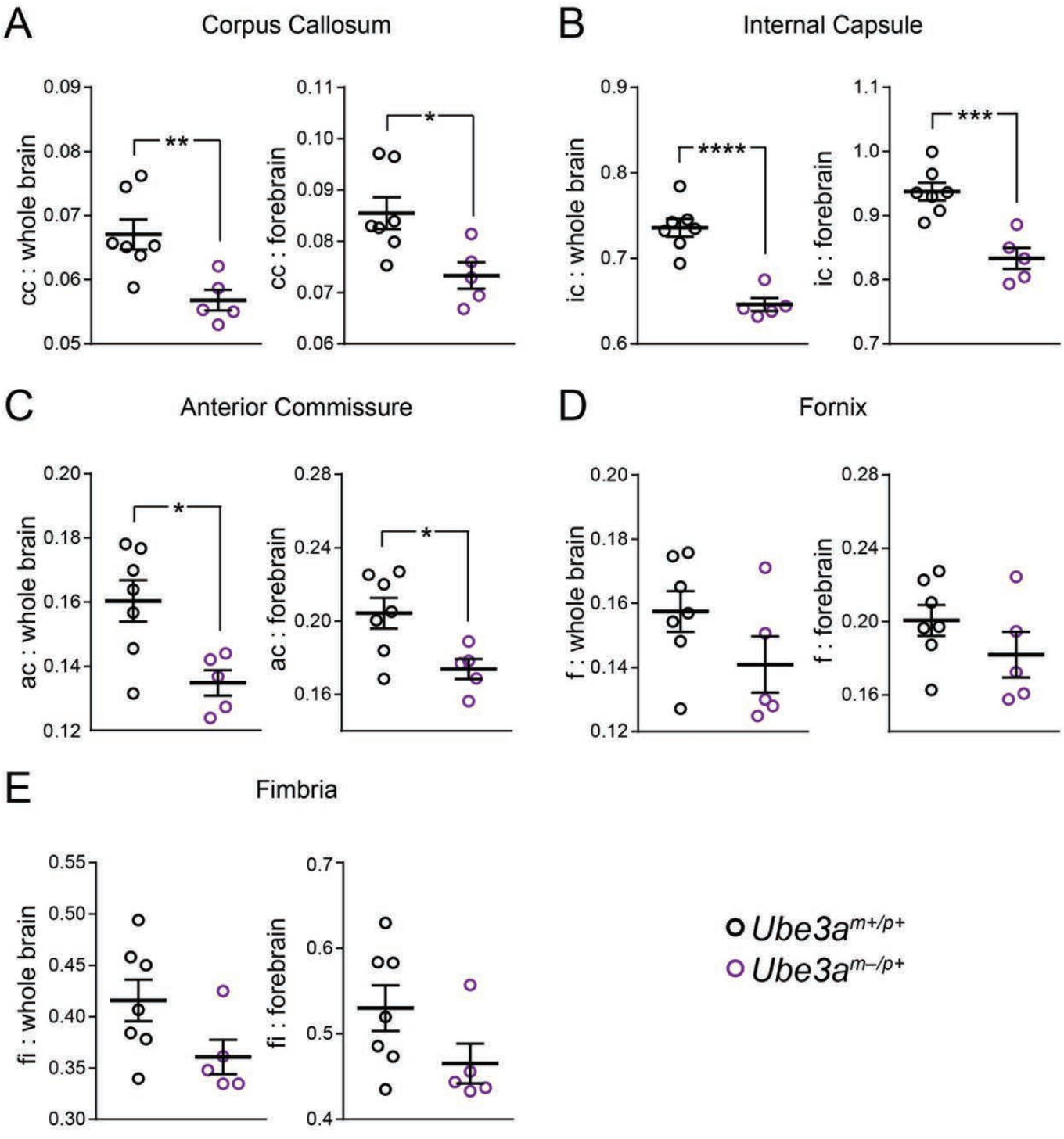

Figure 5. DTI reveals deficits in callosal WM integrity in *Ube3a*$^{m-/p+}$ mice.

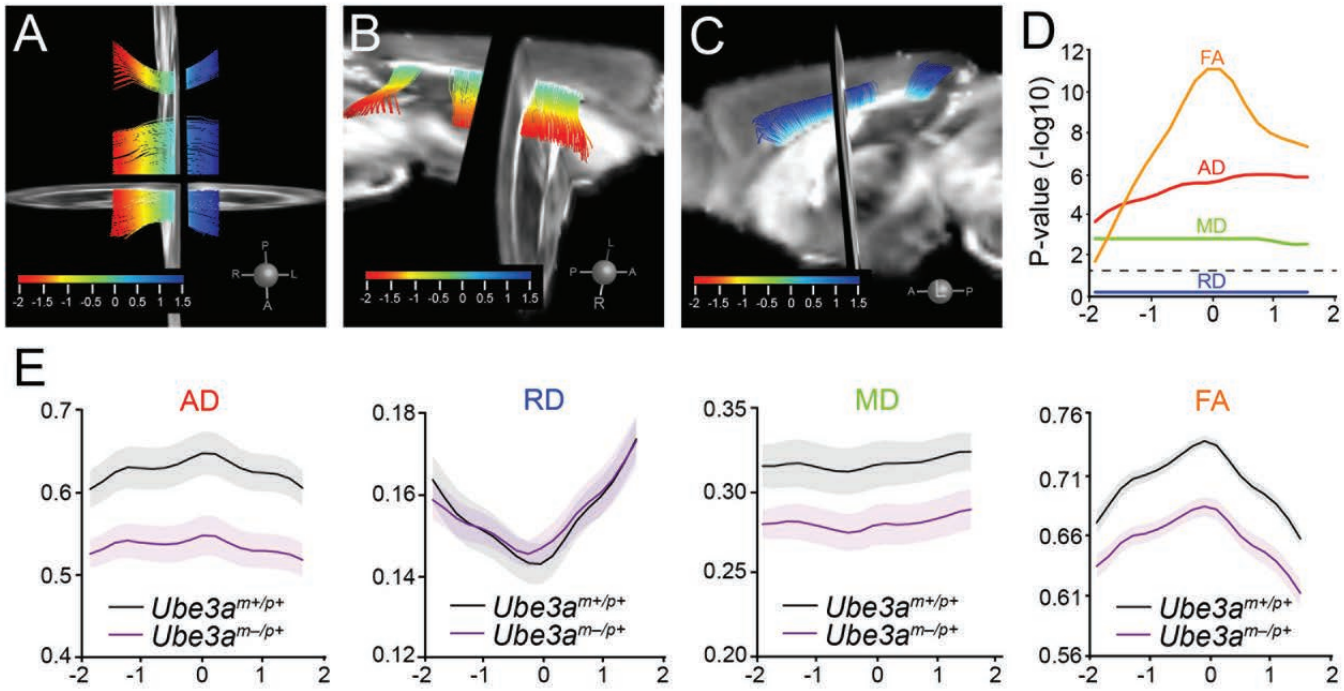

Figure 6. Callosal axons in adult *Ube3a*$^{m-/p+}$ mice display normal myelination but decreased caliber.

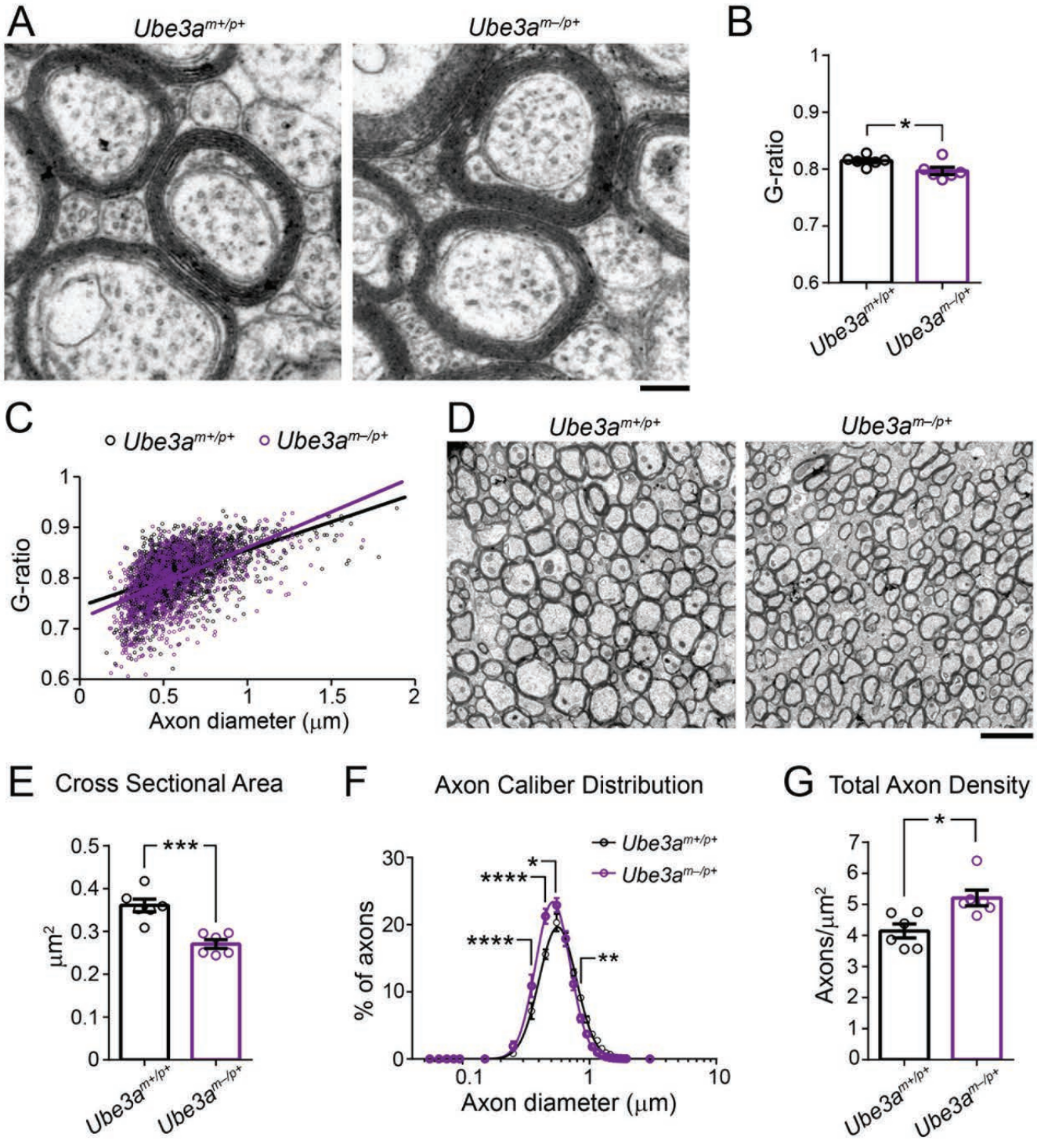

Figure 7. Myelinated callosal axon diameter (linear scale).

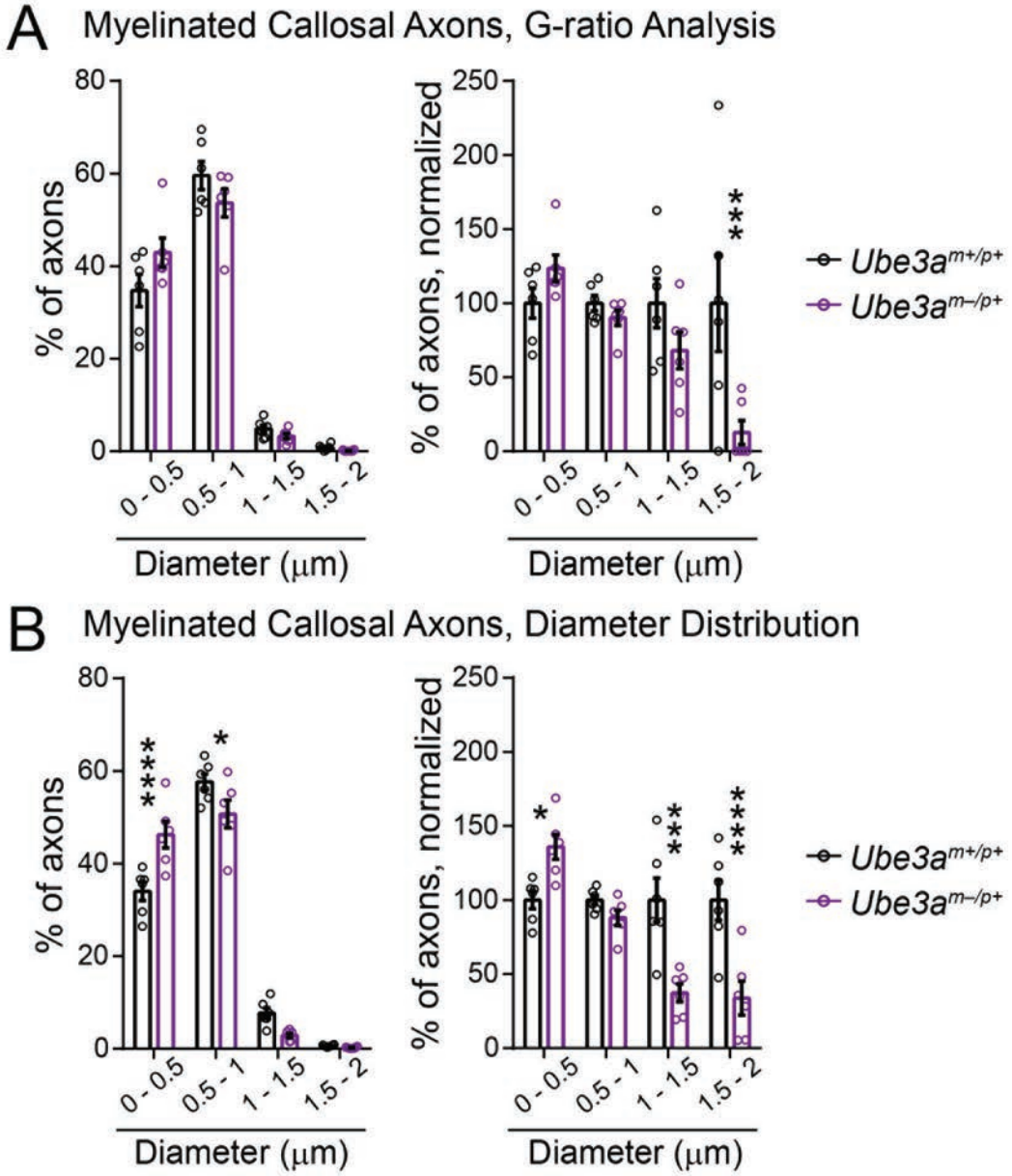

Figure 8. Analysis of unmyelinated callosal axon caliber in adult *Ube3a*$^{m-/p+}$ mice.

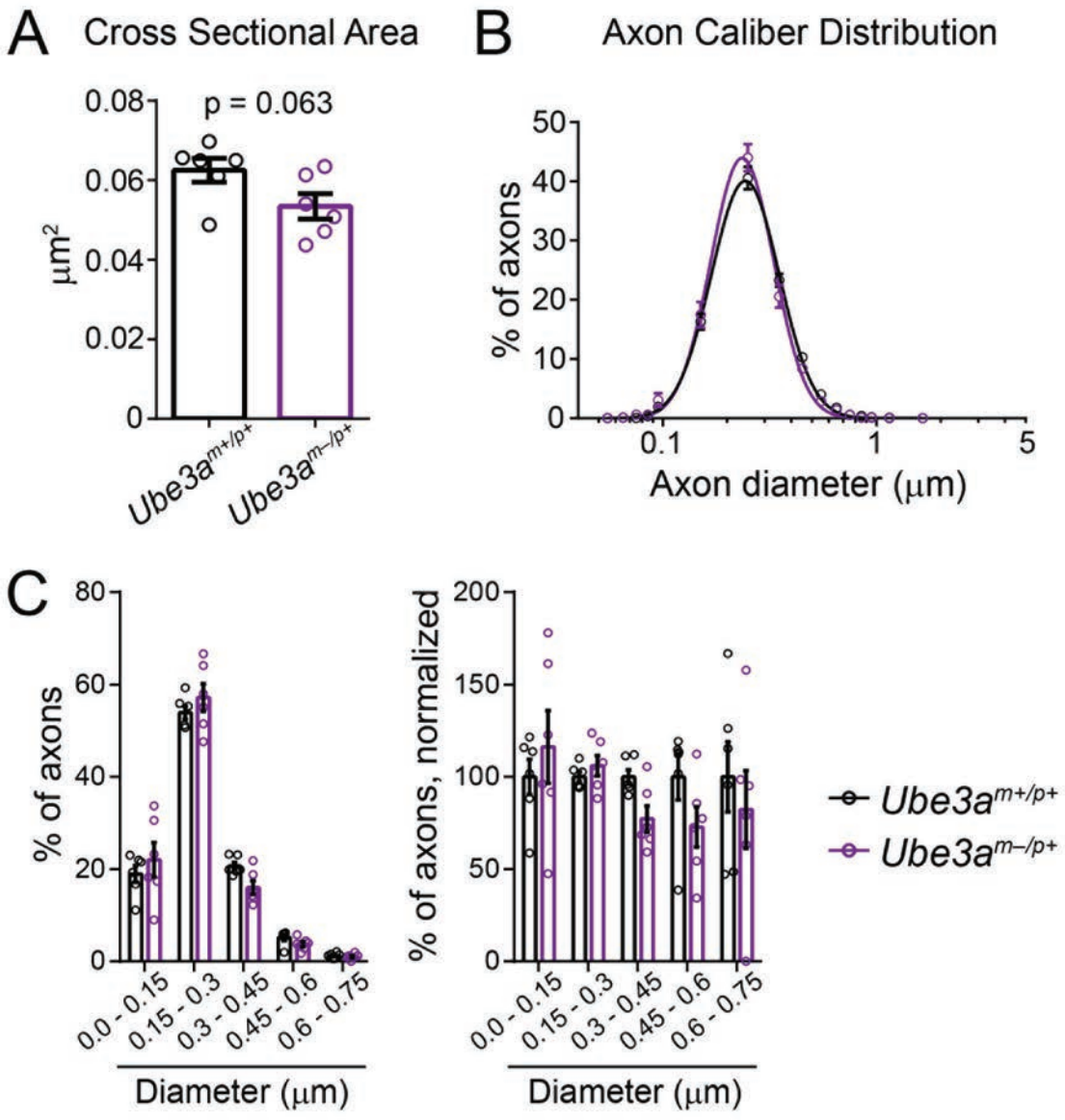

Figure 9. Packing density of cortical neurons is increased in adult *Ube3a*$^{m-/p+}$ mice.

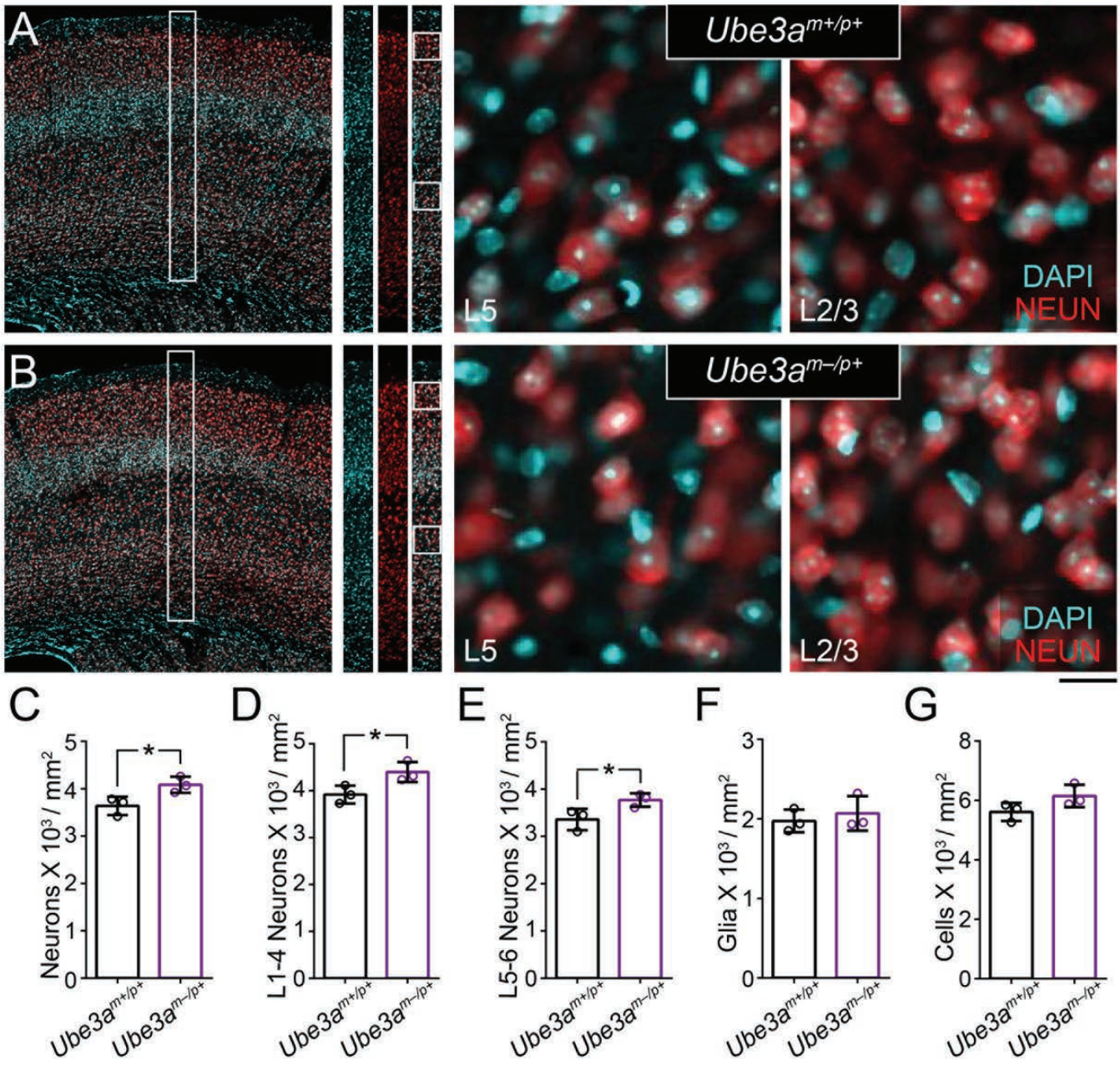

Figure 10. Reduced axon caliber correlates with deficits in sciatic nerve conduction in adult *Ube3a*$^{m-/p+}$ mice.

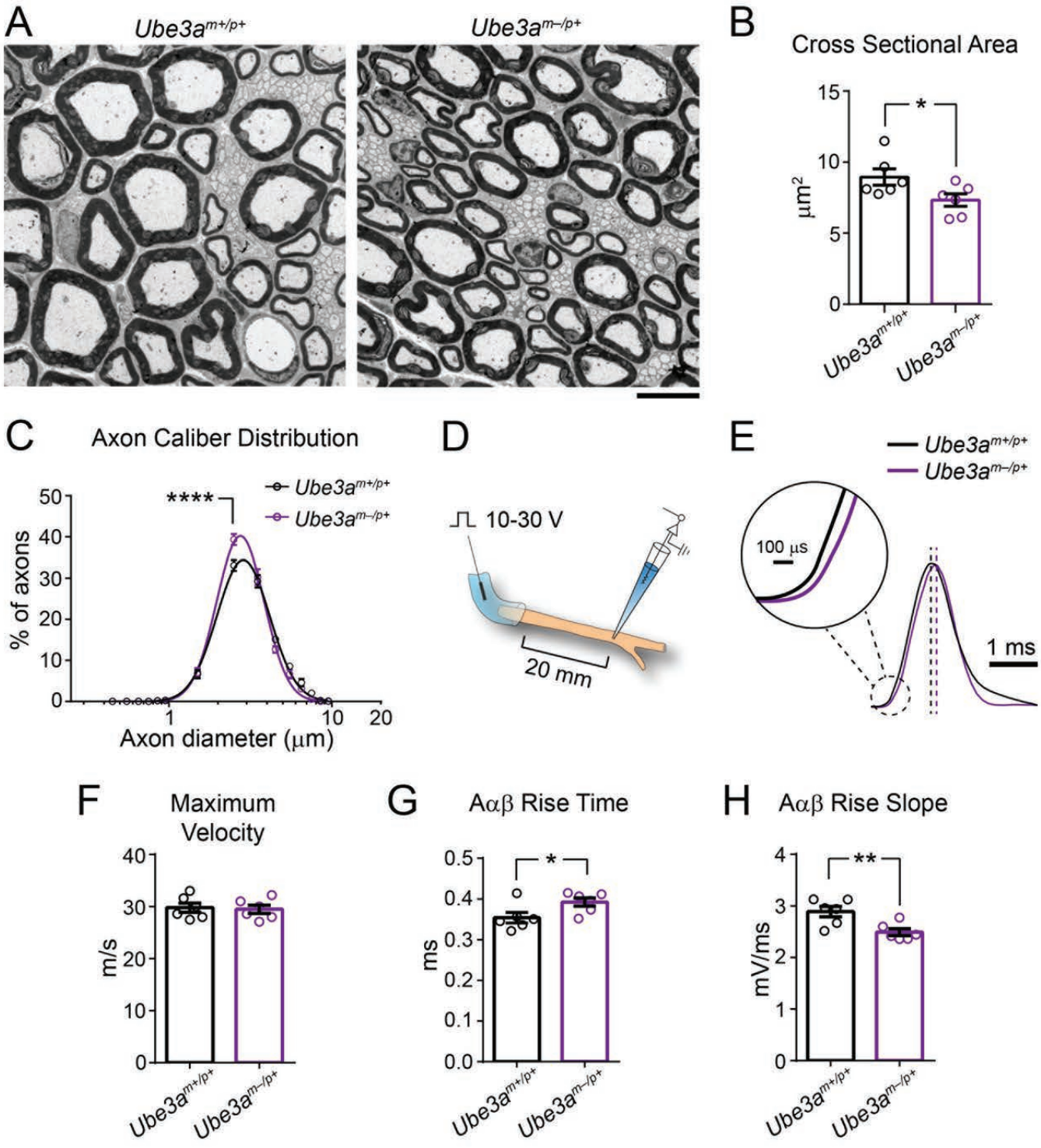

Figure 11. Analysis of g-ratio and diameter (linear scale) of myelinated axons in the sciatic nerve of adult *Ube3a*$^{m-/p+}$ mice.